Centro de Investigación y de Estudios Avanzados del Instituto Politécnico Nacional

DEPARTAMENTO DE FÍSICA

Estudios preliminares para la búsqueda de hadrones exóticos cargados en decaimientos $B^0 \rightarrow K^+ J/\psi\ \pi\pi^0$

Tesis que presenta

Jordan Camilo Correa Rozo

para obtener el Grado de

Maestro en Ciencias

en la Especialidad de

Física

Director de tesis: **Dr. Iván Heredia de la Cruz**

Ciudad de México   Diciembre, 2020

CENTRO DE INVESTIGACION Y DE ESTUDIOS AVANZADOS DEL INSTITUTO POLITECNICO NACIONAL

PHYSICS DEPARTMENT

"Preliminary studies for the search of charged exotic hadrons in $B^0{\rightarrow}K^+J/\psi\ \pi^-\pi^0$ decays"

Thesis submitted by

Jordan Camilo Correa Rozo

In order to obtain the

Master of Science

degree, speciality in

Physics

Supervisor: **Dr. Iván Heredia de la Cruz**

Mexico City

December, 2020.

Agradecimientos

A mi familia, quienes me apoyaron en todos los sentidos y en cada proceso.

A mi director de tesis, Dr. Iván Heredia de la Cruz, por su gran ayuda en la construcción de este trabajo, por su apoyo incondicional y por su infinita paciencia.

A mis sinodales, Dr. Pablo Roig Garcés y Dr. Alberto Sánchez Hernández, que apoyaron en la realización de este trabajo y compartieron sus conocimientos durante estos primeros años.

A los integrantes de la colaboración Belle II en México, que me aconsejaron y apoyaron en cada momento, compartiéndome además su experiencia.

A todos los investigadores y compañeros del departamento de Física del CINVESTAV.

A CONACYT, por el apoyo económico recibido durante la realización de este trabajo.

Acknowledgment

To my family, who support to me everytime.

Resumen

En este trabajo se simuló y reconstruyó el canal exclusivo $B^0 \rightarrow K^+ J/\psi \pi^- \pi^0$, donde se usó el software de Belle II y una muestra genérica de 100 fb^{-1}. Se determinaron las condiciones de optimización sobre un conjunto de variables, donde se obtuvo una buena discriminación entre los eventos de señal y los de ruidos. Además, se identificaron canales de decaimiento con resonancias intermedias y su distribución sobre la masa invariante $m(J/\psi \pi^- \pi^0)$, donde se hará la búsqueda de hadrones exóticos cargados en trabajos futuros. Se obtuvo, a partir de las muestras de ruido simuladas, la eficiencia de selección para $m(K^+ J/\psi \pi^- \pi^0)$, donde se probó que los cortes de selección no modifican el espacio fase asociado a esta variable. Se realizó también un estudio de resolución para estimar, en futuros trabajos, la extensión de las posibles estructuras resonantes sobre el espectro de masa $m(J/\psi \pi^- \pi^0)$, en datos. Finalmente, se compararon las distribuciones generadas por la muestra simulada y una muestra de datos de $\mathscr{L} = (8764.2 \pm 1.5) \ \text{pb}^{-1}$, luego que se blindara una región que contiene el 99.73% de la señal esperada para B^0.

Abstract

In this work, we simulated and reconstructed the exclusive decay $B^0 \to K^+ J/\psi \pi^- \pi^0$ using the Belle II software, together with a generic background sample of 100 fb^{-1}. Optimized selection requirements on a set of variables are determined, leading to good discrimination of signal from background events. Intermediate decay channels were identified and later studied in the invariant mass distribution $m(J/\psi \pi^- \pi^0)$, where the search for charged exotic states will be made in future works. Additionally, the selection efficiency of $m(K^+ J/\psi \pi^- \pi^0)$ was obtained from the simulated background samples, proving that the selection requirements do not modify the phase space associated to this variable. A resolution study on $m(J/\psi \pi^- \pi^0)$ was also made to estimate the extension of possible resonance-like structures in the mass spectrum in data. Finally, we compare distributions between the simulated sample and a data sample of $\mathscr{L} = (8764.2 \pm 1.5)$ pb^{-1}, blinding a region that covers 99.73% of the expected B^0 signal.

Table of contents

List of Figures

List of Tables

1. Introduction

The Standard Model (SM) is considered nowadays as the most complete and successful particle physics theory due to its accurate description of experimental observations and predictive power. QCD theory is included within the SM framework and it considers the Quark Model, where hadrons are made of quarks. All experimental observations on hadrons pointed to a substructure of only 2 or 3 valence quarks. On the other hand, in 2003, the Belle Collaboration observed for the first time a neutral particle X (whose mass is around 3872 MeV/c^2), namely $X(3872)$, in the exclusive decay channel $X(3872) \rightarrow J/\psi\pi^+\pi^-$ [15] and later, collaborations as CDF [16] and LHCb [17] measured its quantum numbers, which do not fit into the conventional $c\bar{c}$-like states despite the presence of the J/ψ particle in its final state. Additionally, it was curious that the mass of X is so close to the mass threshold of the $D^0\bar{D}^0$ pair (with a small difference of ~ 10 KeV) and, therefore, the nature of X could be of molecular type; a weak bound state between two D particles, with 4 valence-quark content, which breaks the paradigm about the existence of hadrons with only 2- or 3-quarks. Later, the BESIII collaboration, in 2013, observed a charged "exotic" particle with mass ~ 3900 MeV/c^2, namely $Z_c(3900)^+$, in the exclusive decay $Z_c(3900)^+ \rightarrow J/\psi\pi^+$, which definitely shows a quark content of $c\bar{c}u\bar{d}$ [18]. More recently, other charged exotic particles have been observed in the charmonium sector, e.g.: $Z_c(4430)^+$ by Belle [19], and $P_c(4380)^+$ and $P_c(4450)^+$ by LHCb [20]. The last two show a minimal quark content of $c\bar{c}uud$ since they were found to decay to the final state $J/\psi p^+$. Thus, the search for exotic states continues and a complete understanding is actually considered as a milestone in particle physics, concerning how quarks and gluons interact.

The Belle II experiment is considered a B factory due to its particle accelerator, SuperKEKB, collides electrons againts positrons at a center-of-mass energy of $\sqrt{s} \sim 10.58$ GeV, just on the top of the $\Upsilon(4S)$ resonance, which normally produces a B meson pair [8]. The cross section for $B^0\bar{B}^0$ productions is $\sigma_{B^0} = 0.510$ nb, which is high enough to search for exotic hadrons decaying from these neutral B mesons (specifically in the charmonium sector). Furthermore, it is highlighted that the Belle II experiment reached the world highest instantaneous luminosity to date and it is expected to increase up to $\mathscr{L} = 8.0 \times 10^{35} cm^{-2}s^{-1}$ within the next few years.

In this work, our main interest is to study the exclusive decay $B^0 \rightarrow K^+X^-$, $X^- \rightarrow J/\psi\pi^-\pi^0$, where it is possible to observe resonant-like structures in the $m(J/\psi\pi^-\pi^0)$ invariant mass distribution and, therefore, the presence of charged exotic states. As a first step, we aim to observe

the decay $B^0 \to K^+ J/\psi \pi^- \pi^0$ and later to explore possible intermediate charged exotic states.

In Chapter 2, it is discussed the theoretical framework of the SM, where elementary particles, oscillation of neutral B^0 mesons and physics beyond the SM will be treated. The different nature and features of the exotic states are briefly explained in Chapter 3, where the most transcendental ones are described and a recent overall status is shown. In Chapter 4, we review the operation of each subdetector in the Belle II experiment and the way in which the BASF2 software simulates collisions through its generators. Results and analysis on simulated events are presented in Chapter 5, where it is also explained how the decay $B^0 \to K^+ J/\psi \pi^- \pi^0$ was generated, which observables were used to discriminate signal from background events and to identify the intermediate resonances that contribute to the same final state, as well as selection efficiency and resolution studies of the invariant mass $m(J/\psi \pi^- \pi^0)$. In Chapter 6 we compare several distributions between the simulated sample and a data sample of $\mathscr{L} = (8764.2\pm1.5)\ \mathrm{pb}^{-1}$. Finally, in Chapters 7 and 8, respectively, we write the conclusions and perspectives for future works.

2. Theoretical framework

The Standard Model (SM) is the most successful theory ever built that describes very accurately three of the four known elementary forces in nature; electromagnetic, weak and strong, excluding the gravitational force that is $\sim 10^{40}$ times weaker than the electromagnetic and whose messenger particle is the graviton which has not been experimentally discovered yet. The SM has three gauge symmetries, building $SU(3)_c \times SU(2)_L \times U(1)_Y$, which are described by Colour, Weak Isospin and Weak Hypercharge symmetries, respectively. Elementary particles can be partially classified by their electric charge, mass and spin, to finally constitute the known leptons, quarks and force carries (gauge and scalar bosons), as shown in Fig. 2-1.

Standard Model of Elementary Particles and Gravity

	three generations of matter (fermions)			interactions / force carriers (bosons)		
	I	II	III			
mass charge spin	≈2.2 MeV/c² ⅔ ½ **u** up	≈1.28 GeV/c² ⅔ ½ **c** charm	≈173.1 GeV/c² ⅔ ½ **t** top	0 0 1 **g** gluon	≈124.97 GeV/c² 0 0 **H** higgs	0 0 2 **G** graviton
	≈4.7 MeV/c² −⅓ ½ **d** down	≈96 MeV/c² −⅓ ½ **s** strange	≈4.18 GeV/c² −⅓ ½ **b** bottom	0 0 1 **γ** photon		
	≈0.511 MeV/c² −1 ½ **e** electron	≈105.66 MeV/c² −1 ½ **μ** muon	≈1.7768 GeV/c² −1 ½ **τ** tau	≈91.19 GeV/c² 0 1 **Z** Z boson		
	<1.0 eV/c² 0 ½ **ν e** electron neutrino	<0.17 MeV/c² 0 ½ **ν μ** muon neutrino	<18.2 MeV/c² 0 ½ **ν τ** tau neutrino	≈80.39 GeV/c² ±1 1 **W** W boson		

QUARKS · LEPTONS · GAUGE BOSONS (VECTOR BOSONS) · SCALAR BOSONS · HYPOTHETICAL TENSOR BOSONS

Figure 2-1.: Elementary Particles in the Standard Model [1].

Leptons and quarks are elementary spin-$\frac{1}{2}$ fermion particles, satisfy the Pauli's exclusion principle and are described by the Fermi-Dirac statistics. On the other hand, the gauge bosons are

elementary integer-spin particles that satisfy the Bose-Einstein statistics and are mediators of the three mentioned interactions; photons for the electromagnetic, gluons for the strong and Z's and charged W's for the weak interactions. Finally, the only scalar boson, the Higgs, is originated in local excitations of the Higgs field. Furthermore, this field is the responsible to provide mass to the elementary particles (except photons and gluons and maybe neutrinos) due to the interaction between matter fields and the Higgs field. [21].

2.1. Leptons

Leptons are spin-$\frac{1}{2}$ fundamental particles divided in three generations. The charged electron (e), muon (μ) and tau (τ) experience the electromagnetic, weak and gravity forces but neutral leptons (neutrinos ν_e, ν_μ and ν_τ) only experience the last two mentioned forces. The same description works for their corresponding antiparticles.

2.2. Quarks

Quarks are spin-$\frac{1}{2}$ fundamental particles and they come in six flavors: u, d, c, s, t, b, which are also divided in three generations. Quarks 'up' (u) and 'down' (d) are the constituents of protons and neutrons and, therefore, the most common hadrons in nature that, together with electrons, make up all visible matter. The other quarks are not common in nature but they are frequently obtained in high-energy physics experiments as particle colliders. Additionally, quarks are never found isolated and they experience all elementary forces. Its electric charge is characterized by being a fraction of the electron charge; $\frac{2}{3}$ for u, c and t and $-\frac{1}{3}$ for d, s and b. In Quantum Chromodynamics (QCD), they are additionally described by the color quantum number (three different types) needed to avoid violation on the Pauli's exclusion principle inside any hadron. Thus, quarks are finally described by two quantum numbers; *flavour* and *color*.

2.3. Hadrons

Hadrons are particles composed by quarks which are constantly interacting, exchanging gluons. The (strong) attraction force among a pair of quarks can be described by the Yukawa's potential, which is very intense for distances on the order of the nucleus size (~ 1.5 fm) and rapidly falls to zero for larger separation. In the quark model, *conventional hadrons* can be classified as **baryons** or **mesons**, depending on the number of constituent valence quarks; three (type-$qqq/\bar{q}\bar{q}\bar{q}$) and two (type-$q\bar{q}$), respectively, with a color combination constrained to be "white" or neutral. This empirical requirement is usually called *color confinement*. In the last two decades, there have been observations of hadrons which seem to have more than three valence quarks; four and five, contradicting the 2- or 3-quarks paradigm. Even so, these "exotic" hadrons can be described within the QCD framework. This topic will be deeply treated in Chapter 3.

2.4. Neutral particle oscillations

Neutral particle oscillation is a phenomenon where a neutral particle is transformed into its corresponding antiparticle owing to flavor-changing weak interactions, e.g.: K^0-$\bar{K}^0$, B^0-$\bar{B}^0$ and D^0-$\bar{D}^0$, in mesonic oscillations. Other well known oscillations are neutrinos' where ν_i can change its leptonic flavour to ν_j, for $i, j = e, \mu, \tau$ and $i \neq j$. This fact shows the existence of *lepton flavour violation* (LFV), which is not discussed in this work but its importance is highlighted in frontier physics.

2.4.1. B^0-$\bar{B}^0$ oscillation

The first observations of B^0-$\bar{B}^0$ oscillations were made by the UA1 collaboration [22], and then by ARGUS [23], both in 1987. In ARGUS, electrons and positrons collide head-on in such a way that $\Upsilon(4S)$ particles are produced and usually decay to $B\bar{B}$ pairs. If neutral B mesons really oscillate, then it is possible to obtain $B^0 B^0$ or $\bar{B}^0\bar{B}^0$ pairs, as it was observed by ARGUS. Later, in 2006, CDF [24] also observed neutral B oscillations, but this time in the system B_s^0-$\bar{B}_s^0$. On the other hand, given a B_q^0 meson (with $q = d, s$), its mass eigenstates; light (L) and heavy (H), can be expressed as a linear combination of flavour eigenstates,

$$|B_{L,H}\rangle = \alpha \left|B_q^0\right\rangle + \beta \left|\bar{B}_q^0\right\rangle, \tag{2-1}$$

where the oscillation frequency correspond to the mass difference $\Delta m = m_H - m_L > 0$ and the total decay width is $\Delta\Gamma = \Gamma_L - \Gamma_H$, with average decay width $\Gamma = (\Gamma_L + \Gamma_H)/2$ [2]. The evolution of a pure $\left|B_q^0\right\rangle$ or $\left|\bar{B}_q^0\right\rangle$ state at $t = 0$ is, respectively:

$$\left|B_q^0(t)\right\rangle = g_+(t)\left|B_q^0\right\rangle + \frac{\alpha}{\beta}g_-(t)\left|\bar{B}_q^0\right\rangle, \tag{2-2}$$

$$\left|\bar{B}_q^0(t)\right\rangle = g_+(t)\left|\bar{B}_q^0\right\rangle + \frac{\beta}{\alpha}g_-(t)\left|B_q^0\right\rangle, \tag{2-3}$$

being the $g_\pm$ factors proportional to the oscillation amplitude; (+) sign for the flavor states remain unchanged and the (-) sign to those which change. In the absence of CP violation in mixing, $|\alpha/\beta| = 1$ and the time-dependent oscillation probabilities become:

$$|g_\pm(t)|^2 = \frac{e^{-\Gamma_q t}}{2}\left[cosh\left(\frac{\Delta\Gamma_q}{2}t\right) \pm cos(\Delta m_q t)\right] \tag{2-4}$$

being $\Delta\Gamma_d/\Gamma_d = (0.001 \pm 0.010)$ and $\Delta m_d = (0.5065 \pm 0.0019)$ ps^{-1} the values reported by the PDG [25]. The neutral B oscillations are produced due to weak interactions at the lowest order, by box diagrams involving two W bosons and two up-type quarks [2], as shown in Fig. 2-2.

$$\bar{b} \quad W^+ \quad \bar{q} \qquad \bar{b} \quad \bar{t} \quad \bar{q}$$
$$t \quad t \qquad W \quad W$$
$$q \quad W^- \quad b \qquad q \quad t \quad b$$
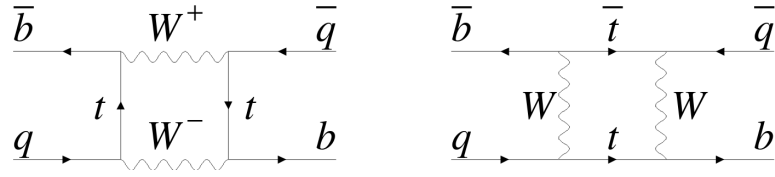
Figure 2-2.: Dominant box diagrams for the $B_q^0 \leftrightarrow \bar{B}_q^0$ transitions (with $q = d, s$) [2]

2.5.   Physics beyond the Standard Model

Despite the SM is the most successful physics model ever built, there are some phenomena that it cannot satisfactorily explain, like the strong CP problem, the nature of dark matter and dark energy, neutrino oscillations (or neutrino mass) and the matter-antimatter asymmetry in the universe. SM also shows inconsistency with general relativity, where one or both theories break down when describing spacetime singularities: the Big Bang and physical singularities. On the other hand, exotics hadrons are contemplated within QCD theory and, therefore, into SM, which means that their existence does not represent signs for new physics but it breaks the paradigm that there are only hadrons with 2- or 3-quarks content. Experimental observations and analysis on them would be very useful to have better understanding about the strong interactions. Thus, in the next chapter we will treat what is an exotic hadron and what are the different types (underlying nature). Additionally, the most transcendental ones will be deeply described and, finally, a recent status will be shown.

3. Exotic hadrons

It was until 1961 when Gell-Mann proposed a successful schematic way to classify the zoo of hadrons found to date, using their electric charge, spin and strangeness quantum numbers; a model called the *eightfold way*. Later, in 1964, Gell-Mann and Zweig postulated independently models to describe hadrons as composite objects, made of elementary particles that Gell-Mann called *quarks*, in such a way that they came in three different types or flavours; $\{u, d, s\}$, and their electric charge would be a fraction of the electron charge [26]. This was based on the flavour symmetry group $\text{SU}(3)_F$. Although quarks had not been experimentally observed, this *quark model* worked well even when additional ones ($\{c, b, t\}$) were added. Furthermore, Gell-Mann classified hadrons in two categories; baryons, with a odd quark content ($qqq/qqq\bar{q}q$, ...), and mesons, with a even content ($q\bar{q}/qq\bar{q}\bar{q}$, ...), keeping the possibility for hadrons with more than 3 quarks, like *tetraquark* and *pentaquark* states. Moreover, QCD contemplates the possibility for more 'exotic' states as those with excited gluon content: qqg (*hybrids*), ggg (*glueballs*), etc., where gluons play a very active role due to their (color) charge and self-interaction [27], unlike photons, in the electromagnetic interactions. A schematic representation of the aforementioned exotic states is shown in Fig. 3-1.
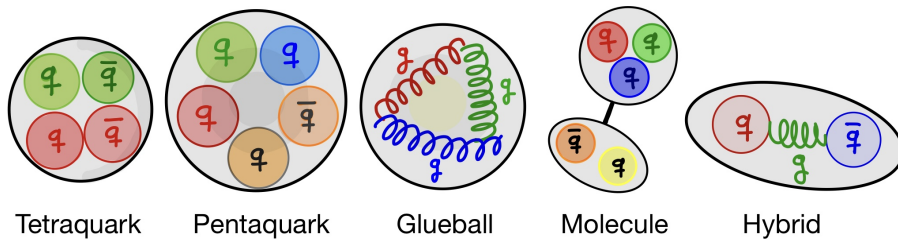
Figure 3-1.: The most common types of exotic hadrons.

Existing models within the QCD framework make an attempt to theoretically describe how quarks and gluons interact and organize inside the exotic hadrons. The most clear classification is shown in Fig. 3-2, where the main categories are Multiquark states and Gluonic excitations. In this work, we focus on the first hypothesis, but a brief description for the Hybrid states is also included. Thus, in this chapter we discuss different ways in which multiquarks states can be classified, what are their main features, which are the most transcendental and, finally, show a recent status of the search for charged exotic hadrons.
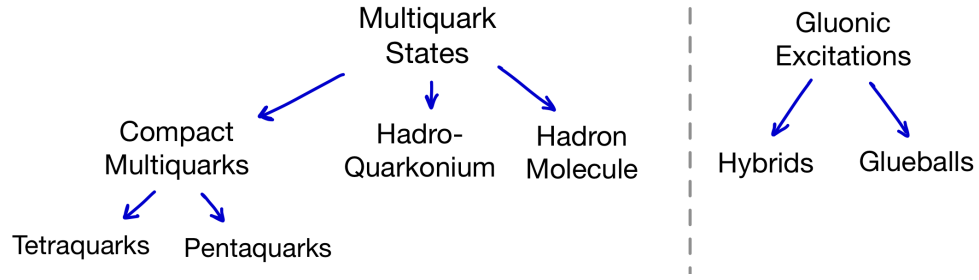
Figure 3-2.: Classification of exotic hadrons [3].

3.1.   Compact multiquarks

Compact multiquark model is the most simple but the most exotic, where quarks (more than three) directly interact exchanging gluons in the same way as conventional 2 or 3 quarks do inside mesons and baryons, respectively. This means that the couplings are strong and, therefore, the mass of the exotic state is considerably larger than the mass threshold (sum of masses) of the daughters involved in any decay channel [28]. *Tetraquarks* ($qq\bar{q}\bar{q}$) and *Pentaquarks* ($qqq\bar{q}\bar{q}$) are included in this model (see schematic representation in Fig. 3-1), where $q = u, d, s, c, b$, excluding the top quark (t) because its lifetime is lower than the hadronization process time. Furthermore, for compact multiquarks it is expected an isospin triplet; neutral and charged versions, where the detected number of events should be twice for the charged version because the conjugate charge decay channel is included. As an additional comment, recently LHCb discovered the first "open-charmed" tetraquark candidate [29], named $X(2900)$ (composed by $ud\bar{s}\bar{c}$ valence quarks) in the decay channel $B^+ \rightarrow D^+ X$, $X \rightarrow D^- K^+$, which was surprising because all previously observed tetraquarks were charmonium or bottomonium-like. Other recent and surprising observation was made also by LHCb for a compact tetraquark candidate, named $X(6900)$, in the invariant mass spectrum of a J/ψ pair, where more than two (heavy) quarks of the same type inside the exotic candidate are inferred; double-charmonium system ($cc\bar{c}\bar{c}$) [30].

3.2.   Hadro-quarkonium

These states are similar to the Hydrogen atom, where a hard core is surrounded by light matter. Here, the core is made of a $Q\bar{Q}$ meson ($Q = c, b$) surrounded by either a light meson ($q\bar{q}$) or a light baryon (qqq) [28]. Each part is constantly interacting with each other by a Van der Waals type force (VDW), what generates a conceptual problem: if the binding force is weak, the system should not remain stable for long enough time to be identified as a well-established state; however, if the force is strong, it is expected that the core and light matter reorganize as a pair of heavy mesons like $D\bar{D}^*$, $B\bar{B}^*$, etc. To date, this conceptual problem has not been theoretically resolved.

3.3. Hadronic molecules

Hadronic molecules are exotic particles similar to the deuterium system ^{2}H, where two hadrons (one proton and one neutron) are binded. For hadronic molecules, an attractive residual VDW force generated by mesonic exchanges (usually pions, but other complementary models include heavier mesons like η's) holds together the constituents in meson-meson or meson-baryon bound states [3]. Furthermore, they are characterized by the closeness between its mass and the mass threshold of their daughters in its most probable decay channel, which implies that the VDW force must be weak.

3.4. Hybrids

They differ from the previous models due to the manifest role of gluonic degrees of freedom. For conventional hadrons and multiquarks hadronic states, quarks interact exchanging gluons in a string-like flux tube in its ground state, where distance between quarks yields to the familiar linear confining potential [3]. On the other hand, in Hybrids, the flux tube is in an excited state with an intrinsic angular moment. In QCD, it is shown that Hybrids can be made of mesons or baryons joined to at least an excited gluon ($q\bar{q}g$ and $qqqg$, respectively), but the meson-gluon state is the most conspicuous because its spin, parity and charge conjugation quantum numbers are not possible for conventional mesons.

3.5. Nomenclature and the most known $c\bar{c}$-like exotic hadrons

After 2003, many other candidates to be exotic particles have been observed, most of them with neutral electric charge. Theorists designed a nomenclature to distinguish the different observed exotic states; XYZ for those containing four quarks; X referring to the ones which are likely $Q\bar{Q}q\bar{q}$ with positive parity (referred as χ_{qJ}(mass) by the PDG naming scheme, where $q = c, b$ and J being the total angular quantum number); Y to those having negative parity and that couple directly to a virtual photon produced in an Initial State Radiation (ISR) process (referred as ψ(mass) by PDG); and finally Z are referred to those charmonium or bottomonium-like states (Z_c and Z_b, respectively), electrically charged and considered as authentic exotic hadrons. On the other hand, for exotic hadrons containing five valence quarks, the nomenclature P_c and P_b is used in analogy to Z states (P_Q(mass), where $Q = c, b$).

Although this nomenclature was used in the last decades, it has been considered to keep only X for denoting all of them and the next ones to be discovered to avoid confusions. Figure 3-3 shows a recent spectrum of states in the $c\bar{c}$ sector (where this work focuses), including those with possible 4-quark content, and excluding those whose quantum numbers are still undetermined.
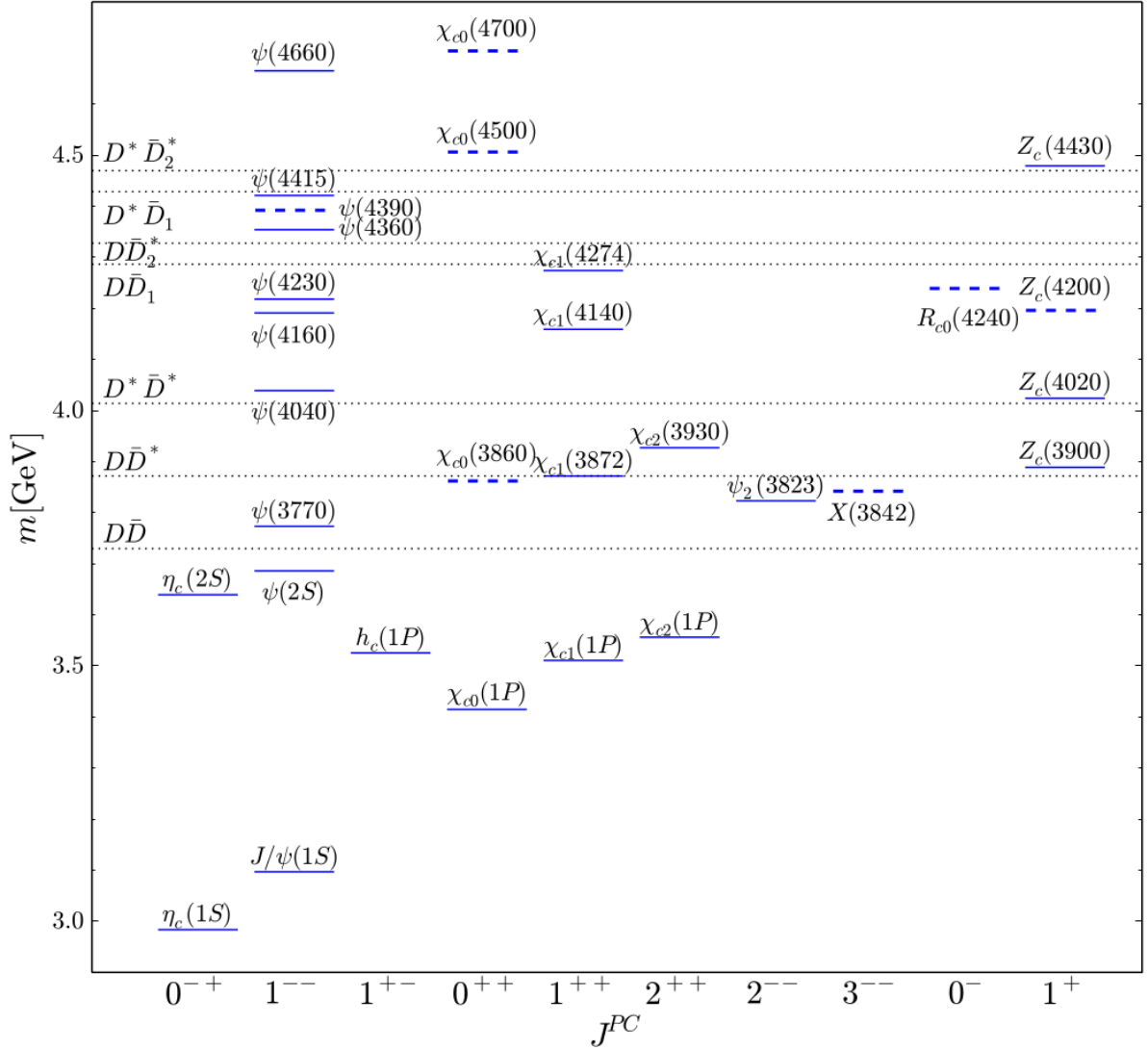
Figure 3-3.: Spectrum of tetraquark states in the $c\bar{c}$ sector as of July 2019. In blue color, solid
lines represent the well-established states (observed in several decay modes) and
dashed lines to those claimed but not established yet. States are labeled according
to the PDG primary naming scheme [3].

As previously mentioned, most of the observed exotic hadrons are electrically neutral in the charmonium spectrum and usually they are found in decays to charged particles in the final state (as happened with $X(3872) \to J/\psi\pi^+\pi^-$), where these final state charged particles are easier to reconstruct in comparison to the neutrals, because they leave well defined tracks in tracking detector (this fact will be deeply treated in section 4.2.1). Then, for these neutral exotic states, how about their charged partners?, would it be possible to observe them?, and if it were possible, what is the most appropriate way to reconstruct them? These and other questions have been around in frontier particle physics during the last two decades and, therefore, they represent a great challenge nowadays. Thus, the main purpose and motivation of this work is the *search for exotic charged partners* of some exotic states previously observed, using the exclusive decay channel $X \to J/\psi\pi^-\pi^0$, where a broad range in the mass spectrum can be analyzed. It is convenient to talk about the most transcendental exotic states with $c\bar{c}$ quark content (some of them showed in Fig. 3-3) to list some important features as their mass M, resonance width Γ, main decay channels and others, from a theoretical and experimental point of view.

3.5.1. $X(3872)$

The neutral $X(3872)$ was discovered in 2003 by the Belle Experiment in the exclusive decay chain $B^\pm \to X(3872)K^\pm$, $X(3872) \to J/\psi\pi^+\pi^-$ [15] and again observed by CDF [16], DØ [31], BaBar [32], LHCb [17] and others. Its world average mass is $M = (3871.69 \pm 0.17)$ MeV/c^2, the upper limit for its narrow resonance width is $\Gamma <$1.2 MeV and its quantum numbers are determined to be $I^G(J^{PC}) = 0^+(1^{++})$ [33]. Additionally, the mass difference for those produced in B^+ and B^0 decays is $\Delta M = (-0.71 \pm 0.96 \pm 0.19)$ MeV/c^2. An attempt to find the charged partners of $X(3872)$ was first made in 2005 by BaBar [32] in the decay $B \to X^-K$, $X^- \to J/\psi\pi^-\pi^0$, and later by other collaborations as Belle in 2011 [34], in the same decay, but they did not find any resonant peak corresponding to a charged $X(3872)^+$ and, to date, it has not been observed. However, upper limits on the production branching fraction were reported.

On the other hand, the underlying nature of the $X(3872)$ is still undetermined, but there are some clues to decipher what it is. First, the idea of being a simple charmonium state was discarded due to the produced pions in $X \to J/\psi\pi^+\pi^-$ came mainly from ρ mesons, in such a way that isospin violation was found, which should be preserved for strong interactions. Later, X seemed to gather the qualities of a molecular state due to its mass proximity to the mass threshold $D^0\bar{D}^{*0}$, whose value is $(1864.38 \pm 0.05) + (2006.85 \pm 0.05) = (3871.68 \pm 0.07)$ MeV/c^2, with a small binding energy of about 10 KeV. However, a recent research showed that the average size of the $X(3872)$ is only slightly larger than that for $\psi(2S)$ ($\sim$1 fm), which corresponds to a typical hadron size, favoring to the compact tetraquark nature [35]. This idea again fails because it is expected for compact multiquarks to have a complete multiplete of charged and neutral states, where the first ones ($X^\pm$) have not been experimentally observed yet, as already

mentioned. Thus, the wave function for this X could correspond to a superposition or mixing of the compact tetraquark and the hadronic molecule states. This shows that the determination of the nature of this exotic candidate is still under investigation and it represents a challenge for the particle physics area.

3.5.2. $Z_c(3900)$

The charged $Z_c(3900)$ was discovered by the BESIII Collaboration in 2013 in the $e^+e^- \to Y(4260) \to Z_c(3900)^{\pm}\pi^{\mp} \to J/\psi\pi^+\pi^-$ decay chain at $\sqrt{s} = 4.26$ GeV [36], being Y(4260) discussed in the next subsection. The actual world average values for its mass and resonance width are, respectively, $M_{Z_c(3900)} = (3887.2 \pm 2.3)$ MeV/c^2 and $\Gamma = 28.2 \pm 2.6$ MeV, and its quantum numbers are determined to be $I^G(J^{PC}) = 1^+(1^{+-})$ [37]. Its neutral partner $Z_c(3900)^0$ was also observed by CLEO-c [38] and BESIII [18] in the decays $e^+e^- \to \pi^0 Z(3900)^0 \to \pi^0(\pi^0 J/\psi)$ and $e^+e^- \to \pi^0(D\bar{D}^*)^0$, respectively, and a recent research showed that $Z_c(3900)^0$ can also come from the exotic $Y(4260)$ which consists of two components; the $Y(4220)$ and $Y(4320)$ [39]. The PDG reports for $Z_c(3900)^0$: $M = (3893.0 \pm 2.3 \pm 19.9)$ MeV/c^2, $\Gamma = (44.2 \pm 5.4 \pm 9.1)$ MeV and $J^P = 1^+$ [37]. It is clear that the $Z_c(3900)$ must have necessarily a $c\bar{c}$ component (charmonium-like, being those neutral electrically) due to the presence of a J/ψ particle in its decay chain. As charged and neutral states have been observed (isospin triplet), the compact tetraquark interpretation is favored. Thus, it is strongly concluded that the $Z_c(3900)$ is an authentic exotic hadron.

3.5.3. $Y(4260)$

This candidate to exotic hadron was observed first by BaBar in 2005 via the ISR process $e^+e^- \to \gamma_{ISR}J/\psi\pi^+\pi^-$ [40] and later it was confirmed by CLEO [41] and Belle [42] collaborations. A recent study about $Y(4260)$ was made by BESIII in 2017 where the cross section for the same decay channel shows that $Y(4260)$ contains two substructures; the $Y(4220)$ and $Y(4320)$, whose masses and resonance widths were measured [43]. BESIII also did studies in different decay channels, $e^+e^- \to \omega\chi_{c0}, \pi^+\pi^-h_c, \pi^+\pi^-J/\psi$ and $D^0 D^{*-}\pi^+ + c.c.$, which were useful to determine a clear $c\bar{c}$ contribution due to the presence of the charmonium-like particles as the χ_{c0}, J/ψ and D. The world average mass and resonance width of the exotic $Y(4260)$ are, respectively, $M = (4230 \pm 8)$ MeV/c^2 and $\Gamma = (55 \pm 19)$ MeV, which are reported by the PDG [44]. Additionally it has been observed a strong correlation among $Y(4260)$, $X(3872)$ and $Z_c(3900)$ due to the observations of the decays $Y(4260) \to \gamma X(3872)$ and $Y(4260) \to \pi Z_c(3900)$, which is a puzzle. On the other hand, it is clear that the $Y(4260)$ cannot be a conventional charmonium state; despite it contains $c\bar{c}$, its mass is above the threshold of $D\bar{D}$, $D\bar{D}^* + c.c.$ and $D^*\bar{D}^*$. A molecular nature seems to be a good choice since the mass of the Y(4260) is just below the threshold of $D\bar{D}_1(2420) + c.c.$ and they can couple in S-wave. The quenched lattice QCD also favors this hypothesis and predicts its quantum numbers to be $J^{PC} = 1^{-+}$ [45]. From

the light-quark model perspective, it was found a not dominant component which estimates a reasonable size of $Y(4260)$, in agreement with the molecular representation [46]. Thus, the nature and properties of the Y(4260) are still an open book.

3.5.4. $Z_c(4430)$

It was first observed by the Belle Collaboration [19] in 2008 in the $\pi^{\pm}\psi(2S)$ mass distribution in the exclusive decays $B \to K\pi^{\pm}\psi(2S)$, confirmed later by LHCb through the same decay channel and in a model independent approach in the $B \to K^{+}\pi J/\psi$ decay [47]. PDG reports its mass and resonance width to be, respectively, $M_{Z_c(4430)} = (4478^{+15}_{-18})$ MeV/c^2 and $\Gamma = (181 \pm 31)$ MeV, as well as the unambiguous Spin-Parity quantum numbers $J^P = 1^+$ [48]. In the same way that $Z_c(3900)$, the charged $Z_c(4430)^+$ is treated as an authentic exotic hadron; specifically one with 4 - quarks content, because knowing its decay channels it is clear that $Z_c(4430)$ must be composed by the quarks $c\bar{c}ud$. A hypothesis considers to $Z_c(4430)$ as the excited tetraquark state of $Z_c(3900)$ due to similar decay channel topologies; $Z_c(4430) \to \pi\psi(2S)$ and $Z_c(3900) \to \pi J/\psi$, being $\psi(2S)$ the first radial excitation state of the J/ψ and it seems more convincing when it is noted that $M_{Z_c(4430)} - M_{Z_c(3900)} = 591$ MeV $\approx M_{\psi(2S)} - M_{J/\psi} = 589$ MeV [36]. On the other hand, the nature of $Z_c(4430)$ has not been easily concluded; from the molecular perspective, it does not seem possible because its mass is not close to any S-wave mass threshold, but from the compact tetraquark perspective there seems to be more hopes. Fabian Goerke and collaborators (in 2016) could reproduce the decay widths for the channels $Z_c(4430) \to \pi\{\psi(2S), J/\psi\}$ in the tetraquark picture [49], using simulations, in agreement with experimental results, implying that a compact tetraquark could be the true nature of this exotic state. Additionally, they predicted the existence of the decay $Z_c(4430)^0 \to D^{*0}\bar{D}^{*0}$ (which have not been still experimentally observed), in addition to its decay rate.

3.6. **Current status and opportunities at Belle II**

The search for exotic hadrons has been one of the milestones for particle physics, being initially motivated by the observation of the neutral $X(3872)$, in 2003, and the subsequent determination of charged exotic states that practically confirm the existence of hadrons with more than three valence quarks. It is important to understand how those exotic hadrons behave, from a theoretical point of view, in such a way that any possible proposed model must match with experimental observations and, therefore, it is important to do preliminary studies. The current status for charged exotic hadrons in the charmonium sector is shown in Table 3-1. The analysis performed in this work will focus in the final state $J/\psi\pi^{\pm}\pi^0$, which corresponds to the second column in that table. The main idea is not to limit ourselves to search only an exotic state, rather, it will be more interesting to explore a broad region in the $J/\psi\pi\pi^0$ invariant mass to search for resonance-like structures in that spectrum.

State	$J/\psi\pi$	$J/\psi\pi\pi^0$	$\psi(2S)\pi$	$\psi(2S)\pi\pi^0$	$\chi_{c1}\pi$	$h_c\pi$	$D\bar{D}$	$D\bar{D}^*$	$\bar{D}^*\bar{D}^*$
$X(3872)^+$	MF	NS	MF	N	MF	MF	N	MF	-
$Z(3900)^+$	S	MF	MF	N	MF	NS	N	S	-
$Z(3930)^+$	MF	N	MF	N	MF	MF	N	N	-
$Z(4020)^+$	NS	N	MF	N	MF	S	N	N	S
$Z(4050)^+$	MF	N	MF	N	S	MF	N	N	MF
$Y(4140)^+$	MF	N	MF	N	MF	N	N	N	MF
$Z(4250)^+$	MF	N	MF	N	S	N	N	N	MF
$X(4350)^+$	MF	N	MF	N	MF	N	N	N	MF
$Z(4430)^+$	NS	N	S	N	MF	N	N	N	MF
$Z(4660)^+$	MF	N	MF	N	MF	N	N	N	MF

Abbreviation	Meaning
S	"seen" (observed)
NS	"not seen" (excluded)
N	"not performed" (analysis not performed)
MF	"missing fit" (spectra published but a fit is missing)
-	forbidden by kinematics or known quantum numbers

Table 3-1.: Status of charged exotic hadrons in the charmonium sector [3].

4. Belle II Experiment

Belle II is a high energy physics experiment located in Tsukuba, Japan, and it came to life with the start of operations of its particle collider, SuperKEKB, which is the update of the KEKB collider. Belle II is expected to improve the performance of previous B-factories (Belle and BaBar), with larger integrated luminosity and better precision in measurements. In this Chapter we discuss the way in which this detector works, the components that make it up and the achievements awarded to this experiment.

4.1. SuperKEKB

SuperKEKB is an asymmetric 7 GeV electron - 4 GeV positron double-ring collider where electrons and positrons collide head-on (deviated by a little angle of 0.0415 rad, respect to the collision axis) with an energy (in the CMS frame) close to the mass of the $\Upsilon(4S)$ (~ 10.58 GeV), which frequently decays to a $B\bar{B}$ ($> 96\%$); therefore, the Belle II experiment is referred to as a B-factory [50]. Figure 4-1 shows the SuperKEKB accelerator scheme. The maximum energy in the CMS frame that the electron - positron pair can reach is ~ 11.24 GeV, which means that the SuperKEKB can produce $\Upsilon(nS)$ particles, with $n = 1, 2, ..., 6$. Heavy particles generated in those collisions usually decay in other lighter states and, finally, they are mostly detected by the different components inside the Belle II detector.

SuperKEKB began operations in February 2016 and it was acknowledged on 21th June 2020 for reaching the world highest instantaneous luminosity of $\mathscr{L} = 2.40 \times 10^{34} cm^{-2} s^{-1}$, surpassing the LHC proton-proton collider record in 2018 of $\mathscr{L} = 2.14 \times 10^{34} cm^{-2} s^{-1}$ [51]. Figure 4-2 shows the maximum reached values for the peak instantaneous luminosity in different experiments along the last five decades.

The Belle II collaboration aims to reach in next few years a peak instantaneous luminosity of $\mathscr{L} = 8.0 \times 10^{35} cm^{-2} s^{-1}$. This means ~ 33 times greater than the current record. To achieve this, it is necessary to reduce the beam cross sectional area around 20 times with respect to the current value and finally obtain a beam area size of 10μm$\times 50$ nm. The "nano-beam" scheme, devised by Pantaleo Raimondi, consists in focusing the very low-emittance beams using powerful magnets at the interaction point (IP), to squeeze the vertical height of the beam [52]. Additionally, it is expected to increase the beam currents by a factor 2.
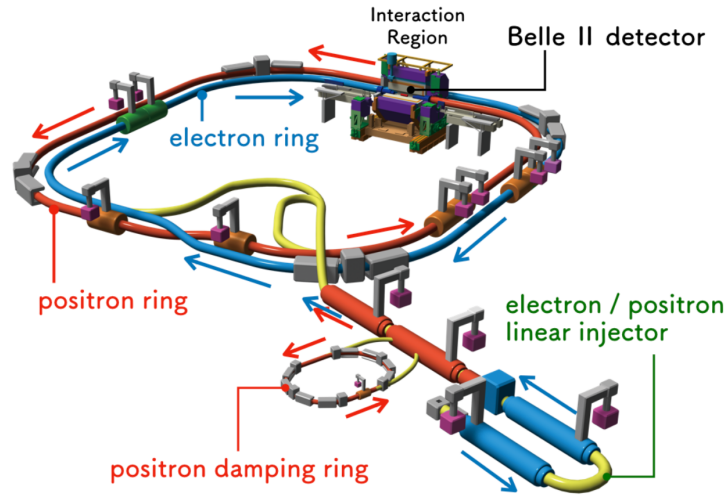
Figure 4-1.: SuperKEKB collider at KEK [4].
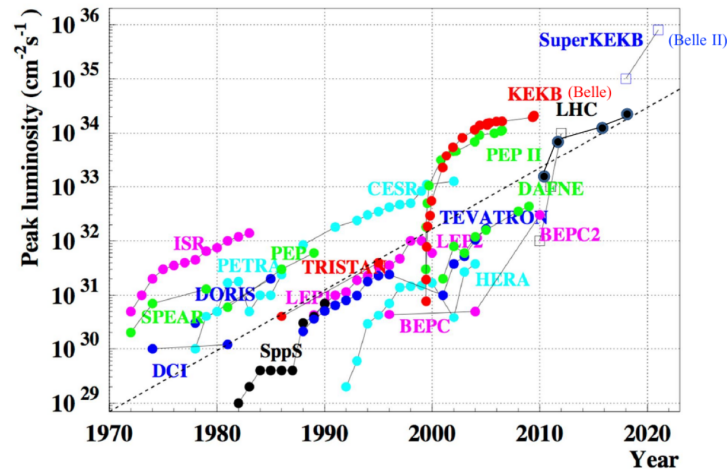
Figure 4-2.: Values for the peak instantaneous luminosity in different experiments along the last five decades [5].

4.2.   Belle II detector

The Belle II detector is a general purpose spectrometer for the next generation B-factory experiment at KEK. This detector is mainly made up of the Tracking detector, the Particle Identification system (PID), Electromagnetic Calorimeter (ECL), K_L-muon detector (KLM), and the Trigger and the Data Acquisition (DAQ) systems. Inside the detector, a generated magnetic field of ~ 1.5T curves the trajectory of the charged particles. Figure 4-3 shows a general scheme of these basic constituents of the Belle II detector and Table 4-1, at the end of this section, summarizes their technical details.
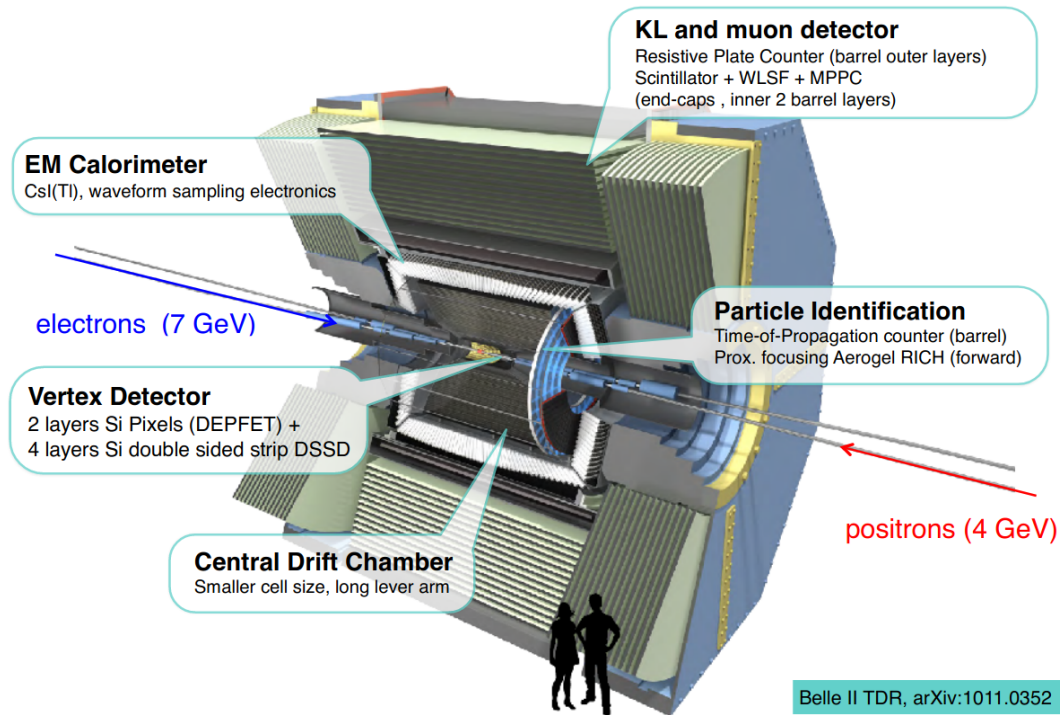
Figure 4-3.: General scheme of the Belle II detector [6].

4.2.1. Tracking detector

The Tracking system is found closest to the IP and its goal is to measure the tracks, decay vertices and momenta of the first produced charged particles. The tracking system must have high resolution to achieve high accuracy in desired measurements. It is composed of the Vertex Detector (VXD) and the outer Central Drift Chamber (CDC), as shown in Fig. 4-3.

Vertex Detector (VXD)

The Vertex Detector is one of the key determinants for the Belle II physics performance. The six-layer detector is made up of the Silicon Vertex Detector (SVD) and Pixel Detector (PXD), which are high-resolution detectors for tracking. The **PXD** is the nearest detection system to the IP. Based on the DEPFET technology, it is made up of 2 cylindrical layers (radii 14 mm and 22 mm) which contain modules, where each module in turn contains 250×1536 pixels that give a real 2D position of the 'hit' left by charged particle with a spatial resolution better than 10 μm and 20 μm for transverse and longitudinal directions, respectively, having a response time of 25 μs. The polar angle where the PXD can reconstruct almost completely the trajectory of tracks is $17° < \theta < 150°$ (it is called $\theta_{comp.}$ in this work), with respect to the beam pipe axis (z-axis) [53].
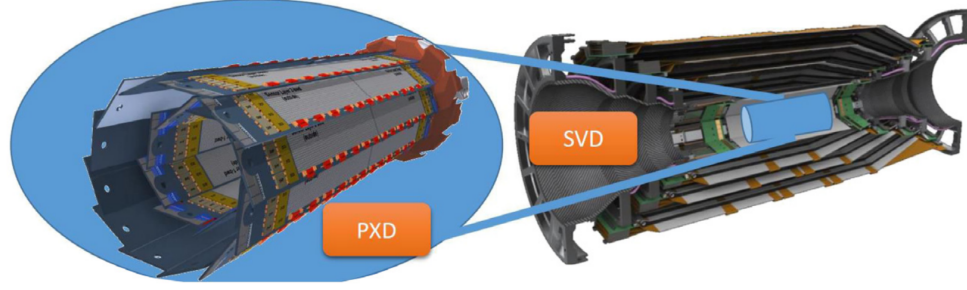
Figure 4-4.: Scheme of the Vertex Detector (VXD), made of the PXD and the SVD [7].

On the other hand, the **SVD** consists of four layers of silicon double-sided strip sensors which are organized in shape of ladders placed at different radii: 39 mm, 80 mm, 104 mm and 135 mm, with respect to the z-axis. These layers cover the same polar angle amplitude as the PXD. For each sensor in any layer, the upper and lower strips are provided in an orthogonal arrangement to give also a 2D position of the 'hit' of the particle, based on the strips that carry the generated electric current from created electron-hole pairs when a reverse-bias voltage is applied to each sensor [54]. Thus, when layers of PXD and SVD are synchronized in detection, it is possible to reconstruct, with high precision, the 3D trajectory of tracks nearest to the IP.

Central Drift Chamber (CDC)

The Central Drift Chamber (CDC) is the main device for track momentum measurements and particle identification. The CDC is found after the VXD and it has cylindrical shape with dimensions 2.3 m-length and 2.2 m-diameter. Inside the CDC, there are 14336 sense wires immersed in a gas which is composed of helium (He) and ethanol (C_2H_6) in a relation $50\% - 50\%$ (see Fig. 4-5) [8]. Thus, when a charged particle traverses the CDC, it gives up a fractional energy $\frac{dE}{dx}$ to the gas to produce ionized electrons attracted by the wires on which a voltage is applied, and finally an electric current is measured. From the function $\frac{dE}{dx}$, it is possible to distinguish among several mass hypotheses, such as pion, kaon, proton and deuterium, as shown in Fig. 4-6. This method is efficient for a momentum range lower than 1 GeV/c.

4.2.2.   Particle Identification (PID)

Belle II is a high-precision experiment and therefore it is important to have a reliable particle identification system, specially for CP violation studies in the neutral B meson system and to suppress background in rare B, D and τ decays. This PID system is made up of the Time of Propagation (TOP) counter in the central region (BRL) and the Aerogel Ring Imaging Cherenkov (ARICH) counter in the forward (FWD) region, both using the Cherenkov radiation (with cone shape) emitted by charged particles when they move faster than the phase velocity of light in that medium [8]. The TOP and ARICH detectors are very efficient to disguish pions from kaons (π/K) for a momentum range lower than 4 GeV/c.
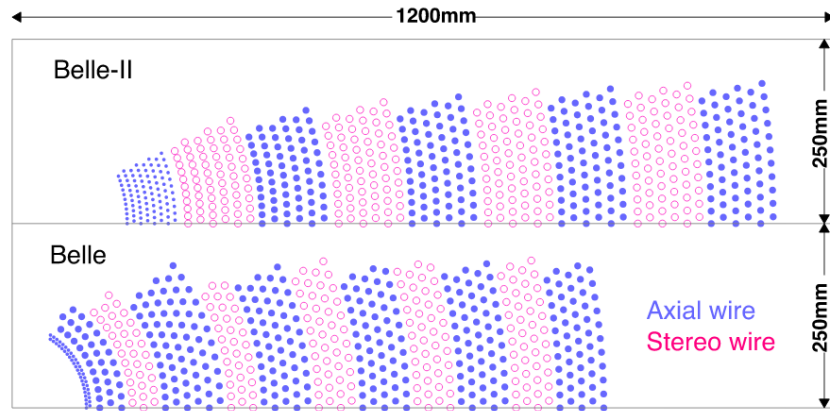
Figure 4-5.: Arrangement of wires inside the CDC. The top configuration corresponds to the Belle II experiment and the bottom one to Belle's. It is remarkable the increasing in the number and density of wires for Belle II to improve the tracking measurements [8].
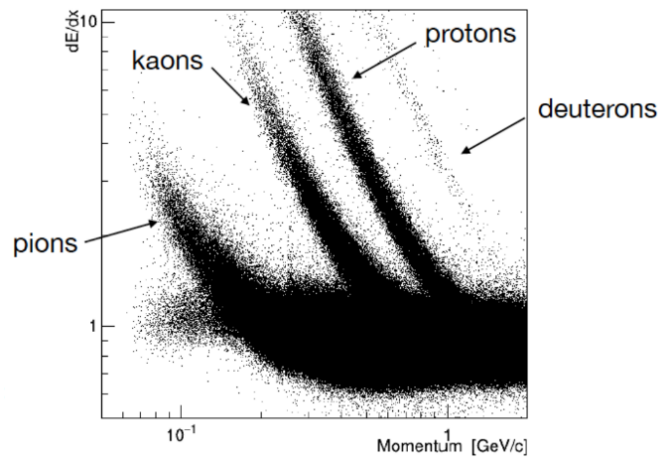
Figure 4-6.: Measurements for $\frac{dE}{dx}$ for several charged particles detected by the CDC [9].
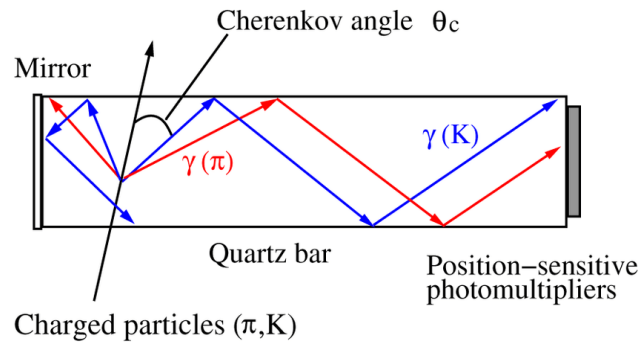
Figure 4-7.: Schematic operation of the TOP detector at Belle II where π/K discrimination is shown [10].

Time of Propagation (TOP)

The TOP detector consists of quartz radiator bars and micro-channel plate photomultiplier tubes located in the barrel region, after the CDC detector. When Cherenkov radiation does propagate through a quartz radiator, it has multiple internal reflections and finally it reaches the photomultipliers tubes at the end of the bars that increase the intensity of the radiation to improve the sensitivity. Photons with different Cherenkov angles reach different photomultiplier channels and arrive at different times [55]. The time and the position convolution are used to obtain the reconstruction of the Cherenkov angle and subsequent discrimination among charged particles. A schematic operation of the TOP detector is shown in Fig 4-7.

Aerogel Ring Imaging Cherenkov (ARICH)

ARICH is a PID detector (for charged particles) which is found in the forward end-cap and it is composed of two aerogel layers which have 2 cm-thickness and different refractive indices; $n = 1.045$ for the one which is nearest to the IP and $n = 1.055$ for the other. This arrangement of refractive-index increasing gives better performance than a single aerogel layer because it focuses Cherenkov-radiation rings. Focused radiation arrives at the Hybrid Avalanche Photo-Detector (HAPD) which has peak quantum efficiency of about 28% at 400 nm and a gain of $\sim 7 \times 10^4$, where radiation is transformed into electric current [56]. Then, different charged particles have different Cherenkov angle and, therefore, signals are detected at different points (rings). Figure 4-8 schematically shows the generated rings for two charged particles (π/K) on the HAPD.
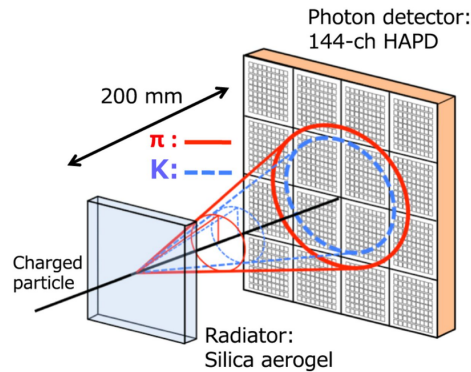
Figure 4-8.: Schematic operation of the ARICH detector at Belle II where π/K discrimination is shown [11].

4.2.3.   Electromagnetic Calorimeter (ECL)

The electromagnetic calorimeter (ECL) is used to detect efficiently photons and electrons in the energy range from 20 MeV to 4 GeV. Additionally, it allows to differentiate electrons from hadrons, particularly pions [8]. The ELC is made up of 8736 CsI(Tl) scintillator crystals just
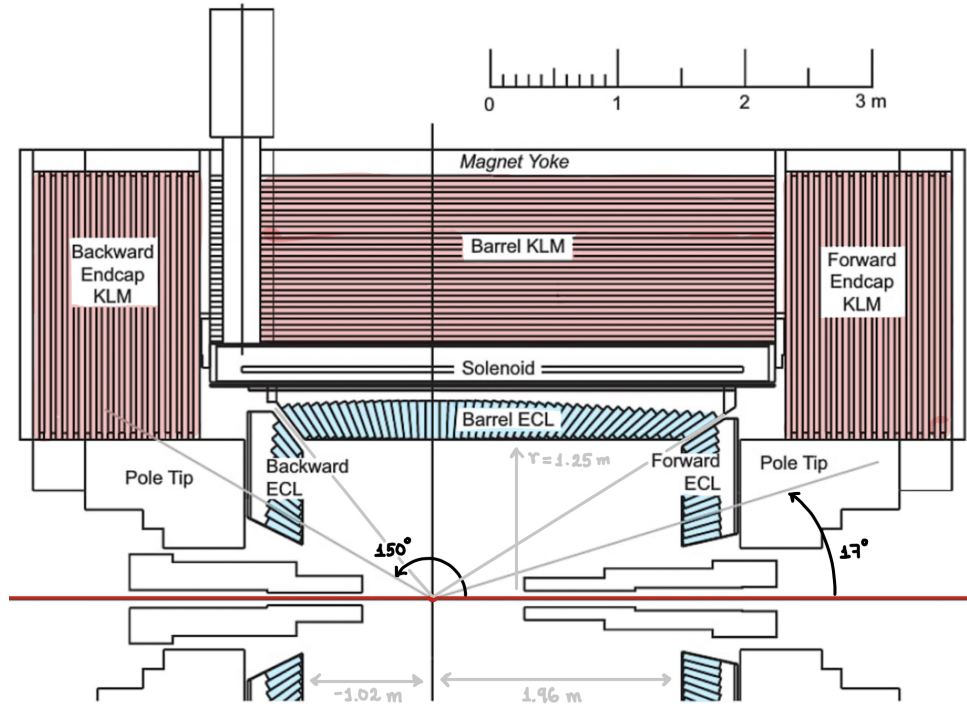
Figure 4-9.: ELC (blue) and K_L-muon (red) detectors at Belle II [12].

like in the Belle experiment, but the electronic readout and software were updated. Each crystal has a 60 mm×60 mm cross section with a 300 mm length, and in their back surface they are attached at two photodiodes, each with a sensitive area of 10 mm × 20 mm. Thus, when electrons traverse these crystals, they have multiple photon-emission processes, and photons have several electron-positron pair productions, in such a way that, in both cases, showers are produced in the crystals, which become electric currents when produced photons interact with the photodiodes, where the Photoelectric effect will take place. Finally, the ECL is found between the CDC and the Solenoid magnets, as is shown in Fig. 4-9.

4.2.4. K_L-muon detector (KLM)

The K_L^0 and muon detector (KLM) consists of an alternative sandwich of 4.7 cm thick iron plates and active detector elements located outside the superconducting solenoid, as shown in Fig. 4-9 [8]. These iron plates return the magnetic flux produced by the solenoid, where this flux can affect the data taken when electronic components are disturbed.

In contrast to Belle, Belle II has to deal with larger background rates, mostly from neutrons produced in showers at the ECL detector from physics processes like radiative Bhabha scattering. On the other hand, the Belle experiment used glass-electrode Resistive Plate Chambers (RPCs), but it pitifully had a long dead time causing a large muon misidentification probability. To

mitigate this problem, RPCs have been replaced in Belle II in the forward and backward endcaps, as well as the three first layers of barrel KLM detector with layers of scintillator strips with wavelength shifting fibers which are tolerant to higher rates and read by silicon photomultipliers to discriminate background rates produced by neutrons. It finally gives a good identification and track reconstruction for muons.

4.2.5. Trigger and Data Acquisition (DAQ)

The trigger system at Belle II has a very important role for data taking. It must be very efficient to discriminate interesting events from background sources which are mainly dominated by Touschek effect, Beam-gas Scattering, Synchrotron radiation, radiative Bhabha process, two-photon process, and beam-beam effects. The scheme of the Belle II trigger system is composed of two levels: hardware, based in a low level trigger (L1), and software, based in a high level trigger (HLT), presenting several improvements compared to its predecessor in Belle and, thus, compensates the increase of background rates produced by the increase in luminosity. Additionally, different trigger algorithms are employed for different topics like τ physics, dark sector searches, two-photon physics, precision measurements of low-multiplicity events and ISR processes, physics beyond standard model and others [14].

The nominal L1 trigger has a latency of 5 μs and maximum trigger output rate of 30 kHz. On the other hand, the HLT must reduce online event rates to 10 kHz for offline storage, and it must identify track regions of interest for PXD readout to reduce data-flux. Finally, the collected data by the DAQ system, which satisfy trigger conditions, are distributed on the GRID system, where real and simulated data are recorded and processed.

To finish this section, the summary of the technical details of the different detection systems at Belle II are shown in Table 4-1.

Measurement	Belle II
B vertex reconstruction (typical)	$\sigma_z = 26$ μm
Tracking	$\sigma_{p_t}/p_t = 0.0011p_t$ [GeV/c] $\oplus$ 0.0025/β
π/K ID	Eff$_K \simeq 0.90$ with Eff$_\pi \simeq 0.04$ for p = 2 GeV/c
Calorimetry	$\frac{\sigma_E}{E} = 7.7\%$ at 0.1 GeV, 2.25% at 1 GeV
Muon-ID	Eff$_\mu$=0.92 - 0.98 with fake rate Eff=0.02-0.06 for p > 1 GeV/c
L1 Trigger	30 kHz max. average rate, Eff$_{hadron} \simeq 1$
DAQ	< 3% dead time at 30 kHz L1 rate

Table 4-1.: Summary of the detector performance [8].

4.3. Belle II Simulation

Simulations basically consist on the generation of e^+e^- collisions, where produced particles decay and interact with the components of the detector over different physics processes. Additionally, beam background simulation is included. The core software is made up mainly of three parts: the Analysis Software Framework 2 (**BASF2**), which contains the Belle II specific code; the **externals**, which contains the third-party code on which BASF2 depends; and, finally, the **tools**, which contain scripts for the software installation and configurations [57].

4.3.1. BASF2

BASF2 is the main software in Belle II which is partitioned into about 40 specific packages which describe each component of the detector and reconstruct objects such as tracks, showers, etc. The source code is written in C++ and is divided in modules which are arranged by the user. This module chain is frequently called *path*. The data processed by each module are stored in a *Data Store*, where any different module can access and modify until the end of the path. The module chain is schematized in Fig. 4-10.
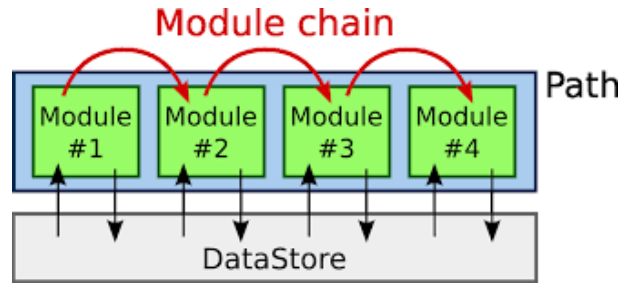
Figure 4-10.: Module chain in BASF2 at Belle II [13].

4.3.2. Generators

Several event generators are used by BASF2 [14], but the most important are: EvtGen, originally developed by BaBar and CLEO which generates and simulates decays of B and D mesons into exclusive final states (specified in a file called *decfile*), where multiple vertices and spin configurations are included, according to the branching ratios of the exclusive decay; PYTHIA and KKMC, used to produce inclusive final states (not included in the decfile) and continuum production of light quark pairs (type-$q\bar{q}$), in addition a their hadronization processes; and, finally, TAUOLA, which simulates τ pair decays (after KKMC production), where spin polarisation effects and transverse spin correlations in τ decays are taken into account. Other useful generators are PHOTOS, which simulates the final state radiation (FSR) correction, mainly dominated by Bremsstrahlung radiation; BABAYAGA.NLO, to simulate radiative Bhabha scattering $(e^+e^- \rightarrow e^+e^-(\gamma))$ and two-photon production $(e^+e^- \rightarrow \gamma\gamma(\gamma))$; and, finally, AAFF,

which includes other low-multiplicity events as $e^+e^- \to e^+e^-\{e^+e^-, \mu^+\mu^-\}(\gamma)$. Table 4-2 summarizes some different physical processes generated by these generators.

Physic process	Cross section [nb]	Selection Criteria	Generator
$\Upsilon(4S)$	1.110 ± 0.008	-	KKMC
$u\bar{u}(\gamma)$	1.61	-	KKMC
$d\bar{d}(\gamma)$	0.40	-	KKMC
$s\bar{s}(\gamma)$	0.38	-	KKMC
$c\bar{c}(\gamma)$	1.30	-	KKMC
$e^+e^-(\gamma)$	300 ± 3	$10° < \theta_e < 170°$ $E_e > 0.15$ GeV in ECL	BABAYAGA.NLO
$\gamma\gamma(\gamma)$	4.99 ± 0.05	$10° < \theta_\gamma < 170°$ $E_\gamma > 0.15$ GeV in ECL	BABAYAGA.NLO
$\mu^+\mu^-(\gamma)$	1.148	-	KKMC
$\tau^+\tau^-(\gamma)$	0.919	-	KKMC
$\nu\bar{\nu}(\gamma)$	0.25×10^{-3}	-	KKMC

Table 4-2.: Physical processes produced by different generators at $\sqrt{s} \sim 10.58$ GeV for e^+e^- simulated collisions in the Belle II experiment [14].

4.3.3. GEANT4

The full detector simulation is made by Geant4 where also background hits and showers are added (beam background overlay). Geant4 simulates the trajectory of each primary particle step-by-step through the different components of the detector and simulates the production of secondary particles from physical interactions between primary particles and atoms of the material, excluding the boson exchange. Furthermore, deposited energy in detectors is calculated. Results are stored in the *DataStore* and are used to reconstruct physical objects.

4.3.4. ROOT

ROOT is a specialized software based in C++ language for data analysis in the particle physics community. Furthermore, output files (*Ntuples*) from the BASF2 reconstruction have ROOT format.

5. Results and Analysis on simulated samples

The objective of this work is to study the exclusive decay chain $B^0 \to K^+ X^-, X^- \to J/\psi\pi^-\pi^0$ in the search for charged exotic hadrons which could be observed in the broad phase space associated to the invariant mass $m(J/\psi\pi^-\pi^0)$. First, we aim to observe the B^0 meson in the decay $B^0 \to K^+ J/\psi\pi^-\pi^0$. As previously mentioned in section 3.5.1, this channel was already explored by BaBar and Belle to search the charged $X(3872)^-$ but, unfortunately, no signal was observed. Knowing this in advance, we suggest to do not limit ourselves to a $m(J/\psi\pi^-\pi^0)$ mass region around 3872 MeV/c^2, but rather, to extend out the range of study to higher (or lower) masses with the hope that known (and possibly new) charged exotic states can be observed. To roughly know how particles (or any decay channel) behave inside the Belle II detector, is convenient to simulate a similar situation and first study it. BASF2 software provides the tools needed to generate and study particles and their decays, step by step, to understand more what is happening inside the detector and later compare with real data. If they match, then we can say that we have a good understanding of the detector and the process under study. After the decay chain reconstruction, we save physical variables to separate, in an optimal way, between signal and background events.

In this Chapter we discussed how the decay chain is generated and simulated in the BASF2 software, what variables and constraints were chosen to separate between signal and background events and how we study the invariant mass, reconstruction efficiency and resolution for $m(J/\psi\pi^-\pi^0)$ under these conditions. Finally, we analyze the found intermediate resonances which lead to the same final state. They must be taken into account to distinguish between known physics and new signals of possible exotic hadrons, when real data be analyzed.

5.1. Signal generation

BASF2 software (release 04-02-08) is used to simulate the decay of interest; the production of $\Upsilon(4S)$ particles from e^+e^- annihilation, such that a pair of neutral B mesons is generated. In the *Signal-side*, the decays $B^0 \to K^+ J/\psi\pi^-\pi^0$, $J/\psi \to (\mu^+\mu^-, e^+e^-)$, $\pi^0 \to \gamma\gamma$ are forced (specified into the *decfile*), imposing 50%-50% production for $J/\psi \to l^+l^-$ in $l = e$ or $l = \mu$, and allowing photon-emission from leptons due to the Bremsstrahlung effect (handled by PHOTOS). On the other hand, in the *Tag-side*, the $\bar{B}^0$ is allowed to decay freely according to the possible decay channels found in the PDG and implemented in EvtGen. Additionally, oscillation of the neutral

B mesons are allowed, which represents a challenge in this analysis and a good approximation to real situations. In this work we only study the decay channel where $J/\psi \to \mu^+\mu^-$, to avoid, for the moment, doing corrections due to Bremsstrahlung radiation (produced mainly by electrons), since those corrections are still being studied by the Collaboration. Finally, a signal sample of $N_{gen} = 10^6$ events is generated to analysis.

5.2. Detector simulation and decay reconstruction

The exclusive decay of interest, specified in the decfile, is generated by EvtGen, and the detector simulation is generated by Geant4, both managed by the BASF2 software [14]. In the last one, several beam background effects (overlay) were included in the simulation: *Beam-gas scattering*, produced by residual gas molecules in the beam pipe which cause changes in the trajectories and energy of electrons due to Coulomb and Bremsstrahlung scattering, respectively; *Touschek effect*, where electrons belonging to the same bunch interact with each other, producing Coulomb scattering; *Radiative Bhabha scattering* ($e^+e^- \to e^+e^-(\gamma)$), where produced photons and electron-positron pairs not belonging to the B meson decays are detected; *Synchroton radiation* (SR), where electrons from the beam lose energy (photon emissions) due to changes in their velocities (acceleration), when a magnetic force (Lorentz force), coming from the powerful superconductor magnets in the ring is applied; and, finally, the *two-photon* processes, where very low momentum electron-positron pairs produced via $e^+e^- \to \gamma\gamma(\gamma) \to e^+e^-e^+e^-(\gamma)$, circle many times inside the detector to produce tracks with snail-like shape. As mentioned in Section 4.3.3, Geant4 leads the produced particles, step-by-step, through the different components of the detector, simulating their trajectory and production of secondary particles.

Once tracks and showers (objects) are produced, we reconstruct the decay of interest (specified into a new file, called *reconstructDecay*) using a set of particle variables and some requirements (cuts) to avoid filtration of a huge amount of background events (to be discussed in the next section), and to select kinematic and geometric regions where the different detectors can do a full reconstruction of these objects. These requirements (called pre-selection cuts) are usually as "soft" as possible to keep the highest number of signal events. These we describe next.

Pre-selection cuts

The energy of photons decaying from neutral pions is required to be higher than 80, 30, 60 MeV in the Forward (FWD), Barrel (BRL) and Backward (BWD) regions in the ECL, respectively, to avoid selecting photons coming from the beam background. Additionally, the 3D and azimuthal angle (on the x-y plane) between the two photons must be lower than 1.5 rad ($\approx 86°$). For reconstruction of neutral pions (π^0), it is required a mass window of $120 < M_{\gamma\gamma}[\text{MeV}/c^2] < 145$, consistent with the PDG mass value of $M_{\pi^0} \approx 134.98$ MeV/c^2. These pre-selection cuts for photons and neutral pions were previously analyzed by T. Koga [58] to obtain a 30% both for

the reconstruction efficiency as purity, defined respectively as:

$$\epsilon := \frac{N_{rec}^{pre}}{N_{gen}}, \tag{5-1}$$

$$purity := \frac{S}{S + B}, \tag{5-2}$$

where N_{rec}^{pre} and $N_{gen} = 10^6$ are the number of reconstructed and generated events (after and previous to the application of the preselection cuts), respectively, and S and B are the total number of signal and background events after cuts.

To select muons from J/ψ and charged K and π from B^0, we use particle identification (also known as **particleID**) variables: muonID, kaonID, pionID, which use information from all available detectors and are defined as:

$$\frac{\mathcal{L}_{<Part>}}{\mathcal{L}_e + \mathcal{L}_\mu + \mathcal{L}_\pi + \mathcal{L}_K + \mathcal{L}_p + \mathcal{L}_d}. \tag{5-3}$$

Here, $\mathcal{L}_{<Part>}$ is the likelihood of being a specific particle from the list $\{e, \mu, K, \pi, p, d\}$. The value used for muons is muonID>0.5, which is the minimum value recommended by the Belle II Collaboration. For charged kaons and pions, we use soft cuts, kaonID>0.1 and pionID>0.1, since these variables have not been efficiently designed so far by the Hadron ID group, but fortunately they offer a decent discrimination for the *swapped* candidates, where charged kaons and pions masses are exchanged, inducing a wrong reconstruction. In Appendix A, we show the distribution for these swapped candidates and how they are practically removed after applying these ID cuts. On the other hand, the chosen mass window for the di-muon candidate is $3.0 < M_{\mu\mu}[\text{GeV}/c^2] < 3.2$, taking into account that the PDG reports $M_{J/\psi} \approx 3.0969 \text{ GeV}/c^2$.

It is required for all final state particles in the decay $(\gamma, \mu, K^\pm, \pi^\mp)$ to cover a polar angle amplitude $\theta_{comp.} = [17°, 150°]$ (on the x-z plane), where the Tracking and ECL detectors can reconstruct completely the objects. For μ, $K^\pm$ and $\pi^\mp$, it was additionally required that their impact parameter components (shorter distance between Track and IP) be $|dz| < 3$ cm and $dr < 1$ cm, corresponding to the z and radial components, respectively. Cuts on dr and dz are necessary since they strongly reduce beam background signals as it is well known that particles not belonging to the decay (except K_L^0, which is not used here) usually have higher values for their impact parameter. Photons which do not come from neutral pions, but come from any other physical processes (mainly from Bremsstrahlung radiation emitted by electrons and muons), are included if $E_\gamma^{not\ \pi^0} > 200$ MeV (a high value to reduce noise coming from the beam). Clearly, it is needed that each event has a minimum of 4 tracks, corresponding to charged particles $\mu(\times 2), K, \pi$ in the signal side (in the extreme case where no final state charged particle is generated in the tag side). Finally, for the neutral B mesons, we use two kinematics

variables calculated in the $\Upsilon(4S)$ CMS: the beam-energy constrained mass M_{bc} and the energy difference ΔE. They are defined as:

$$M_{bc} := \sqrt{(E_{beam}^*)^2 - (\vec{p}_B^*)^2}, \tag{5-4}$$

$$\Delta E := E_B^* - E_{beam}^*, \tag{5-5}$$

where E_B^* and $\vec{p}_B^*$ are, respectively, the reconstructed energy and 3-momentum of each neutral B candidate in center-mass system (CMS) and E_{beam}^* is half the collision energy e^+e^-, also in the CMS. It is preferable to use M_{bc} instead of the simple reconstructed B^0 mass (from the 4-momenta of its daughters, without the beam energy constraint) because it improves the resolution on these measurements. Pre-selection cuts on these kinematic variables are respectively, $M_{bc} > 5.0$ GeV/c^2 and $|\Delta E| < 0.4$ GeV, taking into account that $M_{B^0} \approx 5.280$ GeV/c^2 from the PDG. Once pre-selection cuts are established, the reconstructDecay file is run on BASF2 to produce *root* files to be analyzed. This process is discussed later in section 5.4.

5.3. Background analysis

When electrons and positrons collide head-on, several event types are produced; those from $q\bar{q}$ ($u\bar{u}$, $d\bar{d}$, $c\bar{c}$, $s\bar{s}$), $B^0\bar{B}^0$ (mixed), B^+B^- (charged) and $\tau^+\tau^-$ (tau-pair), called *generic*, in addition to those which have *low multiplicity* (few tracks); $e^+e^- \to e^+e^-(\gamma)$, $e^+e^- \to \mu^+\mu^-(\gamma)$, $e^+e^- \to e^+e^-\mu^+\mu^-(\gamma)$, and others. These event types are considered as background samples, as they may mimic the signal that we have already generated, and they are also simulated by BASF2 and placed on the storage elements of the Belle II Grid. As described before, these samples include the detector simulation and beam background overlay.

Within the Belle II collaboration, the production of these samples correspond to the Thirteenth official MC campaign (MC13a), using the release 04-02-08. The integrated luminosity used in this analysis for each event type (mixed, charged, $u\bar{u}$, $d\bar{d}$, ...) is $\mathcal{L} = 100$ fb^{-1}. Only generic background samples are included in this work because low multiplicity events do not pass our preselection. Remaining combinatorial background found in our signal samples (after the decay reconstruction), is neglected and, in fact, completely removed after applying the selection requirements.

5.4. Selection optimization

Once pre-selection cuts are established on some variables and *root* files are generated, we need to apply additional cuts to discriminate signal from background events in an optimal way. Additional variables are considered, some of them related to the kinematic of the particles (as invariant masses and momenta), but also those related with the event shape, which we describe in detail in this section. Our first goal is to observe a clear signal of the $B^0 \to K^+ J/\psi \pi^- \pi^0$ decay

reflected in the B mass distribution (remembering that the main objective is the observation of $B^0 \to K^- X^+$, being $X^{\pm}$ a charged exotic state). Then, we focus mainly on cleaning the variables M_{bc} and ΔE. Therefore, it is necessary to apply tighter cuts on those variables we have already used and to appeal to new ones in such a way that the Punzi function (usually called *Figure of Merit* or simply FOM) reaches its maximum value [59]:

$$FOM(\epsilon_T, B) = \frac{\epsilon_T}{a/2 + \sqrt{B}}, \tag{5-6}$$

where $\epsilon_T := N^{sel}_{rec}/N_{gen}$ is the (total) reconstruction efficiency, N^{sel}_{rec} and B are the number of reconstructed signal events and the total number of background events (sum on generic samples) after applying selection cuts and, finally, $a \approx 1.6449$ is a constant related with the confidence level (90% CL). The variables used for selection (to maximize the FOM) and requirements on them are shown in Table 5-1:

$(p_t)^*_{\gamma\gamma} > 0.3$ GeV/c	$(p_t)^*_K > 0.2$ GeV/c	$p^*_{\mu\mu} < 1.35$ GeV/c
$0.120 < M_{\gamma\gamma}(\text{GeV/c}^2) < 0.139$	$3.06 < M_{\mu\mu}(\text{GeV/c}^2) < 3.12$	FoxWolframR2 < 0.54

Table 5-1.: Used variables in optimization and requirements on them. (*) symbol is referred to the CMS and the subscript t to transverse (momentum).

To find these final selection requirements (which we call *Optimized cuts*), we use an algorithm that applies a series of cuts on the variables and select those that maximize the FOM. Upper and lower cuts on these variables are treated independently. The algorithm is iterated to verify if initial cuts can be improved. In Table 5-1 the FoxWolframR2 is defined in terms of the Fox-Wolfram momentums (l-component):

$$H_l = \sum_{i,j=1}^{N} \frac{|\vec{p}_i||\vec{p}_j|}{s} P_l(cos(\Omega_{ij})), \tag{5-7}$$

where s is the total energy of the event, $cos(\Omega_{ij}) = cos\theta_i cos\theta_j + sen\theta_i sen\theta_j cos(\phi_i - \phi_j)$, P_l are the Legendre polynomials and N is the number of involved particles (denoted by the i and j indices) in the event. When a event is jet-like, particles have high momenta, and $\sum |\vec{p}_i||\vec{p}_j| \lesssim s$ and $cos(\Omega_{ij}) \gtrsim 0$, in such a way that $H_l \lesssim 1$; in the opposite case, when the event is spherical-like and the particles moves in all directions, then $H_l \sim 0$ [60]. FoxWolframRl refers to the ratio H_l/H_0; in particular FoxWolframR2 $= H_2/H_0$. Figures 5-1 and 5-2 show the optimization cuts (red vertical lines) applied to the variables used for selection (only for the first loop) in an ordered way; firstly those which strongly discriminate signal from background events. As noted, the lower cut on $M_{\gamma\gamma}$ is equal to that in preselection. Moreover, from FoxWolframR2< 0.54, it could be deduced that the event shape tends to be spherical as usually happens in B decays. As an additional comment, the β factor on plots is only used to weight the signal distribution to have similar height as the background distributions, but it does not have any physical meaning.
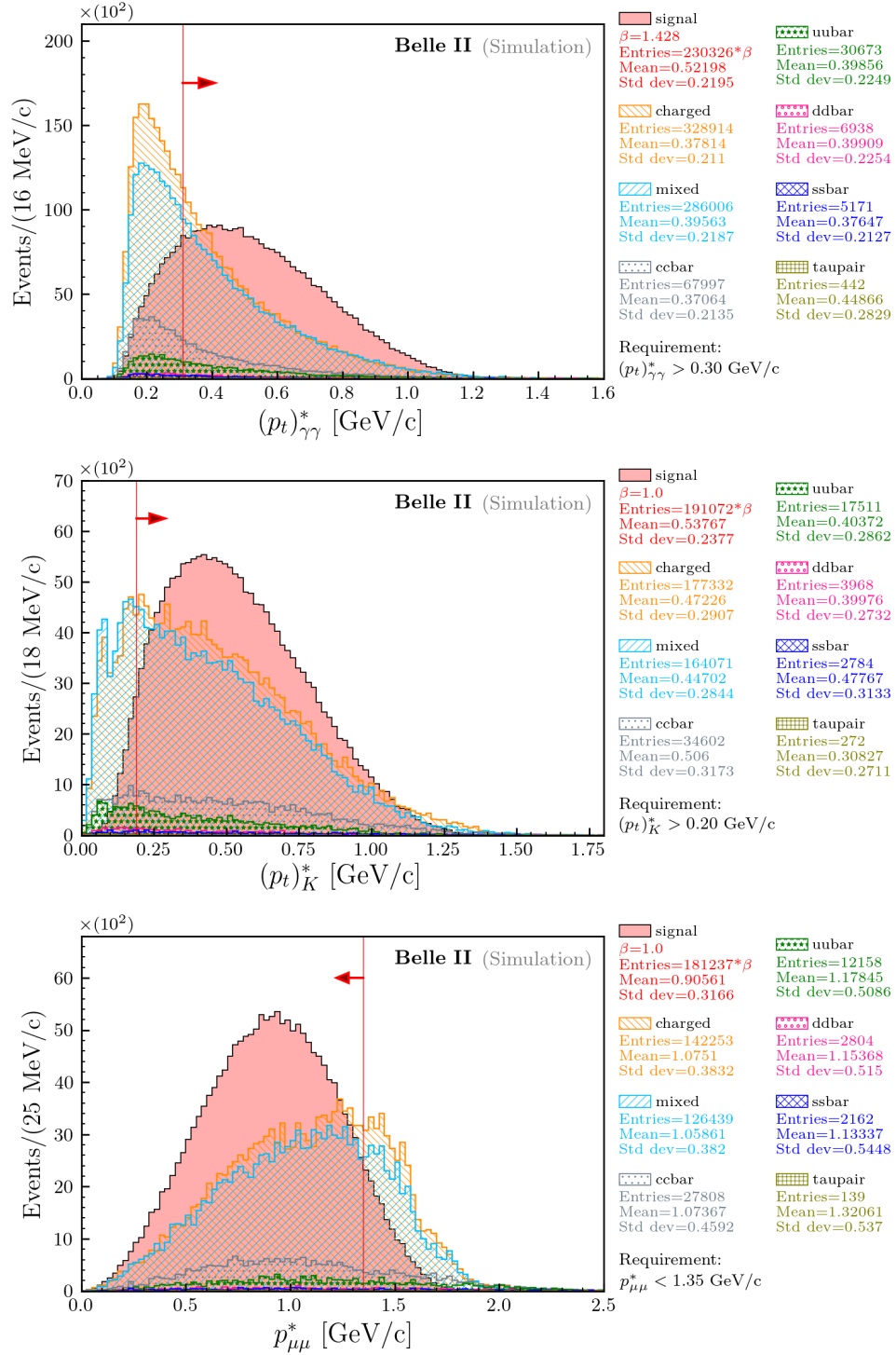
Figure 5-1.: Optimization requirements applied to momentum distributions measured in the CMS. Shown are the transverse momentum of the di-photon (top) and charged kaons (middle) and the total momentum of the di-muon candidates (bottom).
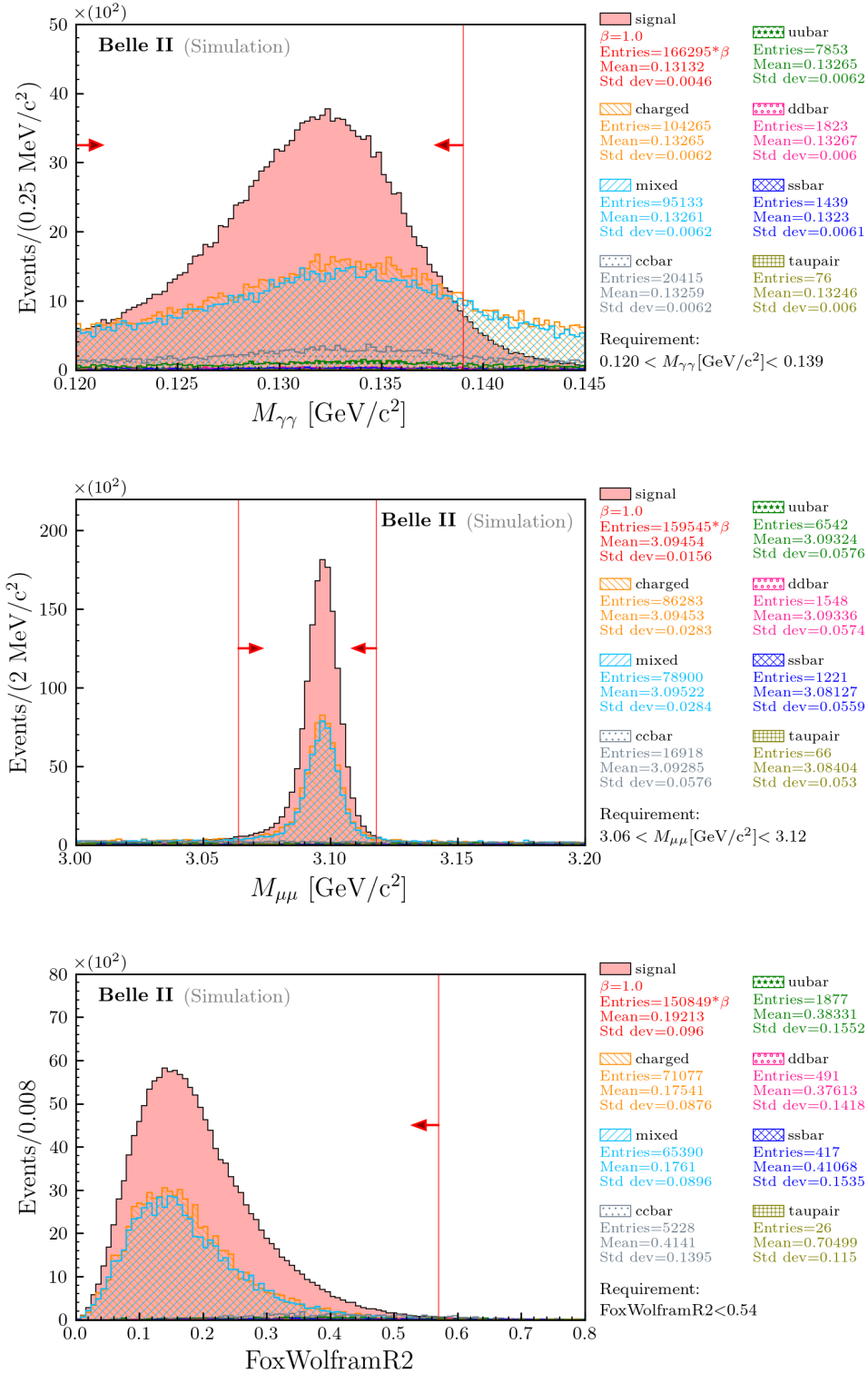
Figure 5-2.: Optimization requirements applied to mass distributions of reconstructed particles; di-photon (top) and di-muon (middle) candidates, and FoxWolframR2 (bottom), related with the event shape.

5.5. FOM analysis

The cuts previously shown on the variables are applied in an organized way such that the FOM (described in Eq. 5.6) grows up until reaching a plateau. It is important to remember that maximixing the FOM leads to optimal cuts to discriminate signal from background events. The final value obtained for the total reconstruction efficiency is $\epsilon_T \approx 14.8\%$. ϵ_T is useful to estimate how many signal events are expected in data when these optimization cuts are applied. Figure 5.3 shows the FOM and the number of signal and background events as a function of the cuts applied on each variable after several iterations.
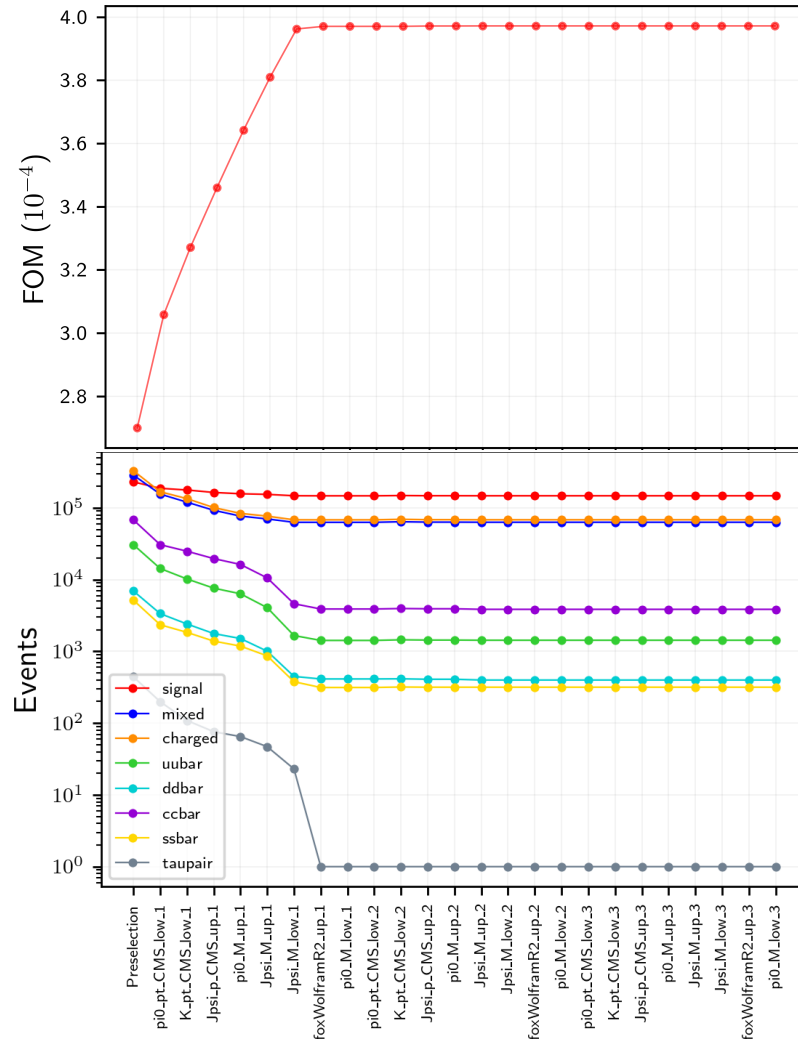
Figure 5-3.: Evolution of the FOM (top) and number of entries for signal and background events (bottom) as a function of the cuts applied on each variable. Subscripts 'up' and 'low' refer to upper and lower cuts, respectively, and the numerical label at the end of each variable corresponds to the iteration number (loop).

As noted from the bottom plot in Fig. 5-3, the first cut on FoxWolframR2<0.54 removes almost completely the $\tau^+\tau^-$ events (from 26 to 1), which are usually jet-like. Thus, it is highlighted the importance of using this variable even when it seemed unpromising (see bottom plot in Fig. 5-2). Finally, Fig. 5-4 shows M_{bc} and ΔE_{B^0} distributions after applying the optimization cuts.
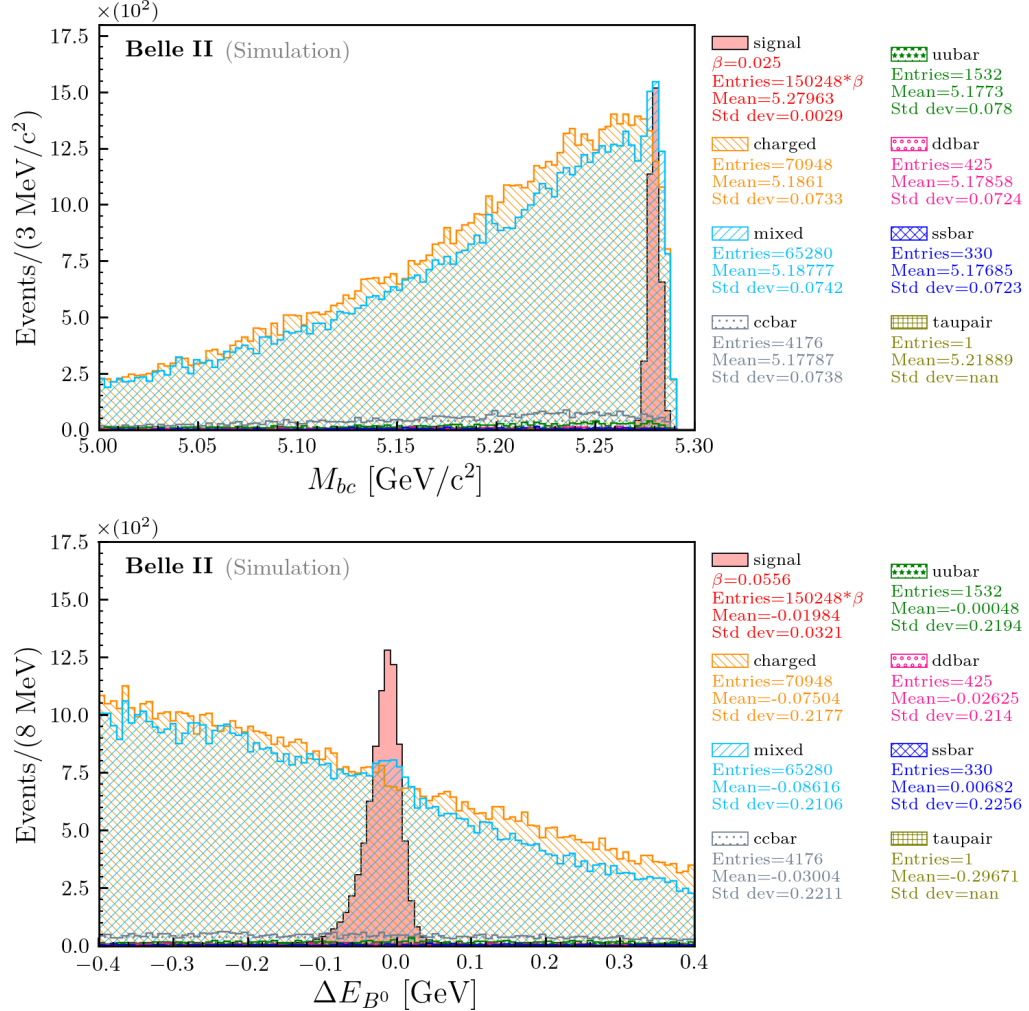
Figure 5-4.: Beam-energy constrained mass M_{bc} (top) and energy difference ΔE (bottom) for neutral B^0 mesons after applying optimized cuts shown in Table 5-1.

It can be observed that around 5.280 GeV/c^2 for M_{bc} and 0 GeV for ΔE_{B^0}, slight peaks emerge from the background level only for mixed type. These are mainly produced by the existence of intermediate decay channels (or intermediate resonances) which leads to the same 6-particles final state ($B^0 \to K^+(\mu^+\mu^-)\pi^-(\gamma\gamma)$). In the next section, we show how these intermediate resonances manifest individually on the $m(J/\psi\pi^-\pi^0)$ distribution. In a future analysis, we will perform a 2D fit on M_{bc} and ΔE_{B^0} (or 3D fit, adding to $m(J/\psi\pi^-\pi^0)$) to model the signal events and later, to apply cuts on them to obtain a cleaner distribution for $m(J/\psi\pi^-\pi^0)$, in

order to facilitate the observation of peaks from possible exotic states.

5.6.   Intermediate resonances

The observation of these slight peaks on M_{bc} and ΔE_{B^0} shows that there must be intermediate resonances that produce the same 6-particle final state that we considered so far. Some collaborations could identify some of those resonances, but in this work we investigate others too. Table 5-2 shows the intermediate resonances found only in the mixed background. For example, BaBar [32] and Belle [15, 61] studied the channels of the type $B^0 \to J/\psi K_X^0$ (where K_X^0 designates any neutral excited kaon that decays to $K^+\pi^-\pi^0$, such as $K_1(1270)$ and $K_2^{*0}(1430)$; type ②, ⑥, ⑦ and ⑧) and $B^0 \to J/\psi K^{*0}$ decays combined with a random pion. However, radiative processes as ③, ⑨ and ⑩ have not been considered in other analysis.

Figure 5-5 shows the $m(J/\psi\pi^-\pi^0)$ distributions for processes ①-⑧ in an organized way, excluding ⑨ and ⑩ because they have a very low number of entries. Appendix B shows the distributions for these contributions on M_{bc} and ΔE_{B^0}. Separately, these contributions do not produce resonance-like structures in the $m(J/\psi\pi^-\pi^0)$ distribution (except very slightly ①) but, besides, most of them produce peaks on the M_{bc} and ΔE_{B^0} distributions around 5.280 GeV/c^2 and 0 GeV, respectively, (in the same way the signal does), except ③ that present a smearing in M_{bc} and a shifting in ΔE_{B^0} due to the photons emitted by Bremsstrahlung effect and, ④ and ⑤ that present both shifting and smearing only on ΔE_{B^0}, which could occur by a random combination with particles from the other side.

Label	Decay channel	Entries
①	$B^0 \to J/\psi K^{*+}(892)\pi^-$, $K^{*+}(892) \to K^+\pi^0$	167
②	$B^0 \to J/\psi K_1^0(1270)$, $K_1^0(1270) \to \rho^-K^+$, $\rho^- \to \pi^-\pi^0$	141
③	$B^0 \to \chi_{c1}(1P)K^+\pi^-\pi^0$, $\chi_{c1}(1P) \to J/\psi\gamma$	53
④	$B^0 \to \psi(2S)K^{*0}(892)$, $\psi(2S) \to J/\psi\pi^0$, $K^{*0}(892) \to K^+\pi^-$	42
⑤	$B^0 \to \psi(2S)K^+\pi^-$, $\psi(2S) \to J/\psi\pi^0$	31
⑥	$B^0 \to J/\psi K_2^{*0}(1430)$, $K_2^{*0}(1430) \to \rho^-K^+$, $\rho^- \to \pi^-\pi^0$	22
⑦	$B^0 \to J/\psi K_2^{*0}(1430)$, $K_2^{*0}(1430) \to K^{*0}(892)\pi^0$, $K^{*0}(892) \to K^+\pi^-$	25
⑧	$B^0 \to J/\psi K_2^{*0}(1430)$, $K_2^{*0}(1430) \to K^{*+}(892)\pi^-$, $K^{*+}(892) \to K^+\pi^0$	20
⑨	$B^0 \to \chi_{c2}(1P)K^+\pi^-\pi^0$, $\chi_{c2}(1P) \to J/\psi\gamma$	6
⑩	$B^0 \to \psi(2S)K^+\pi^-\pi^0$, $\psi(2S) \to \chi_{c1}(1P)\gamma$, $\chi_{c1}(1P) \to J/\psi\gamma$	1

Table 5-2.: Decay chain with intermediate resonances contributing to the $J/\psi\pi^-\pi^0K^+$ final state in the mixed background.
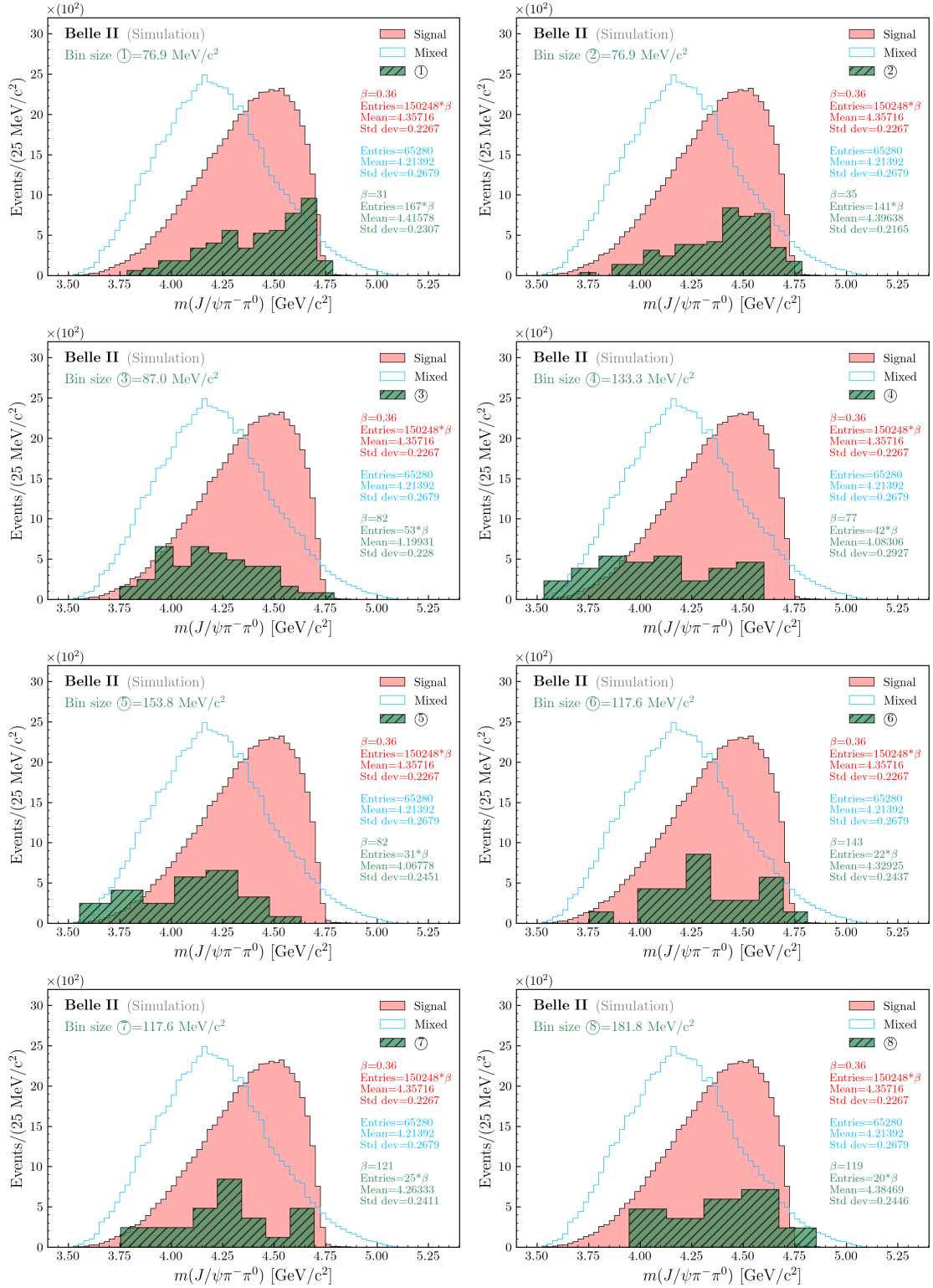
Figure 5-5.: Major signal contributors for the $B^0 \rightarrow J/\psi \pi^- \pi^0 K^+$ decay on the mixed background (see Table 5-2) projected on the $m(J/\psi \pi^- \pi^0)$ distribution. Optimized cuts in Table 5-1 are already applied.

Misunderstood decay channels with a high number of entries are also found and shown in Table 5-3. Moreover, Figure 5-6 shows the distributions of these on $m(J/\psi\pi^-\pi^0)$ and Figures B-3 and B-4 in Appendix B, on M_{bc} and ΔE_{B^0}, respectively. These decay channels are not found in the PDG decay list and, therefore, we believe they probably are produced by combinations with random particles (i.e. from the tag-side). The first of them, referred as Ⓐ, could be explained by the presence of a ρ^- decaying to $\pi^-\pi^0$ generated by a oscillated B^0 in the tag-side. The same situation for Ⓑ, where neutral pions possibly come from the tag-side. The kinship among particles is established by using *mcPDG* variables on codes. These variables give the PDG number of particles only in an upward or downward way; father and grandfather in the first case, and son and grandson in the second case. However, the mcPDG variables cannot give information about brothers or uncles. This fact makes it difficult to reject wrong combinations; how to know if a particle really comes from a B^0 in the signal-side or from an oscillated B^0 in tag-side using only mcPDG variables?. The rejection of the misunderstood decay channels is expected to be improved in future works with new Monte Carlo matching algorithms.

Label	Decay channel	Entries
Ⓐ	$B^0 \to J/\psi K^+ \rho^-,\ \rho^- \to \pi^-\pi^0$	422
Ⓑ	$B^0 \to J/\psi K^{*0}(892)\pi^0,\ K^{*0}(892) \to K^+\pi^-$	209

Table 5-3.: Misunderstood decay channels contributing to the $B^0 \to J/\psi\pi^-\pi^0 K^+$ final state in the mixed background.
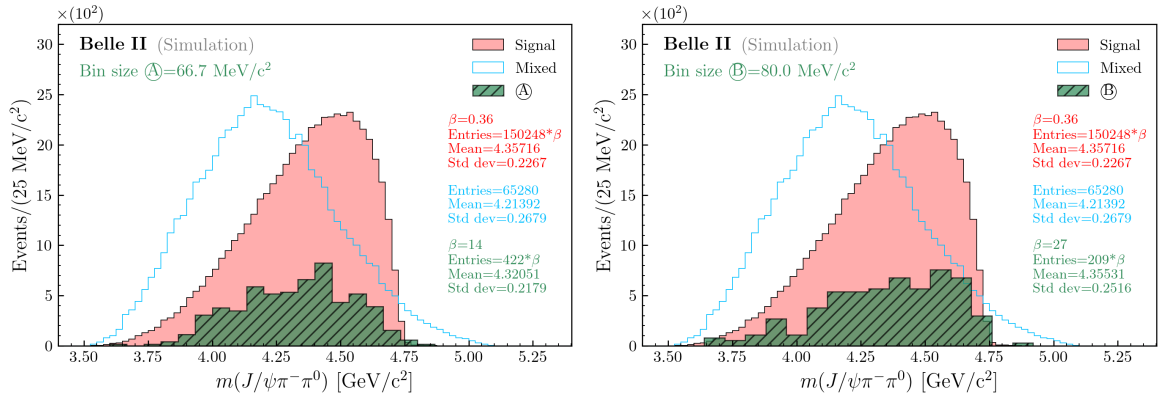
Figure 5-6.: Distributions for the misunderstood decay channels that contribute to the $B^0 \to J/\psi\pi^-\pi^0 K^+$ final state in the mixed background projected on the $m(J/\psi\pi^-\pi^0)$ distribution.

Finally, Figure 5-7 shows how M_{bc} and ΔE_{B^0} look when the decays with intermediate resonances, shown in Tables 5-2 and 5-3, are rejected (after applying the optimization cuts). It can be noted

that peaks produced near to 5.280 GeV/c^2 and 0 GeV for M_{bc} and ΔE_{B^0}, respectively, disappear almost entirely once these 1139 events of mixed background are discarded. Additionally, 28 events for signal were also discarded when these intermediate decay channels were rejected, showing that, possibly, in the free decaying for $\bar{B}^0$ in the tag-side, it was also obtained the same 6-particle final state and, therefore, it was identify as signal events. Thus, it is concluded that it has been found the most of decays with intermediate resonances (found or not in the PDG decay list) which are unwanted (or must be taken into account) for a future 2D fit on M_{bc} and ΔE_{B^0} (or 3D fit if $m(J/\psi\pi^-\pi^0)$ is added).

Figure 5-7.: Beam-energy constrained mass M_{bc} (top) and the energy difference ΔE_{B^0} (bottom) for neutral B^0 mesons after applying the optimized cuts (shown in Table 5-1) and when the decays with intermediate resonances (shown in Tables 5-2 and 5-3) are rejected.

Figure 5-8.: Selection efficiency for $m(J/\psi K^+\pi^-\pi^0)$ when optimized cuts (see Table 5-1) are applied. True momenta are used for reconstruction and the decay channels, shown in Table 5-2, are excluded.
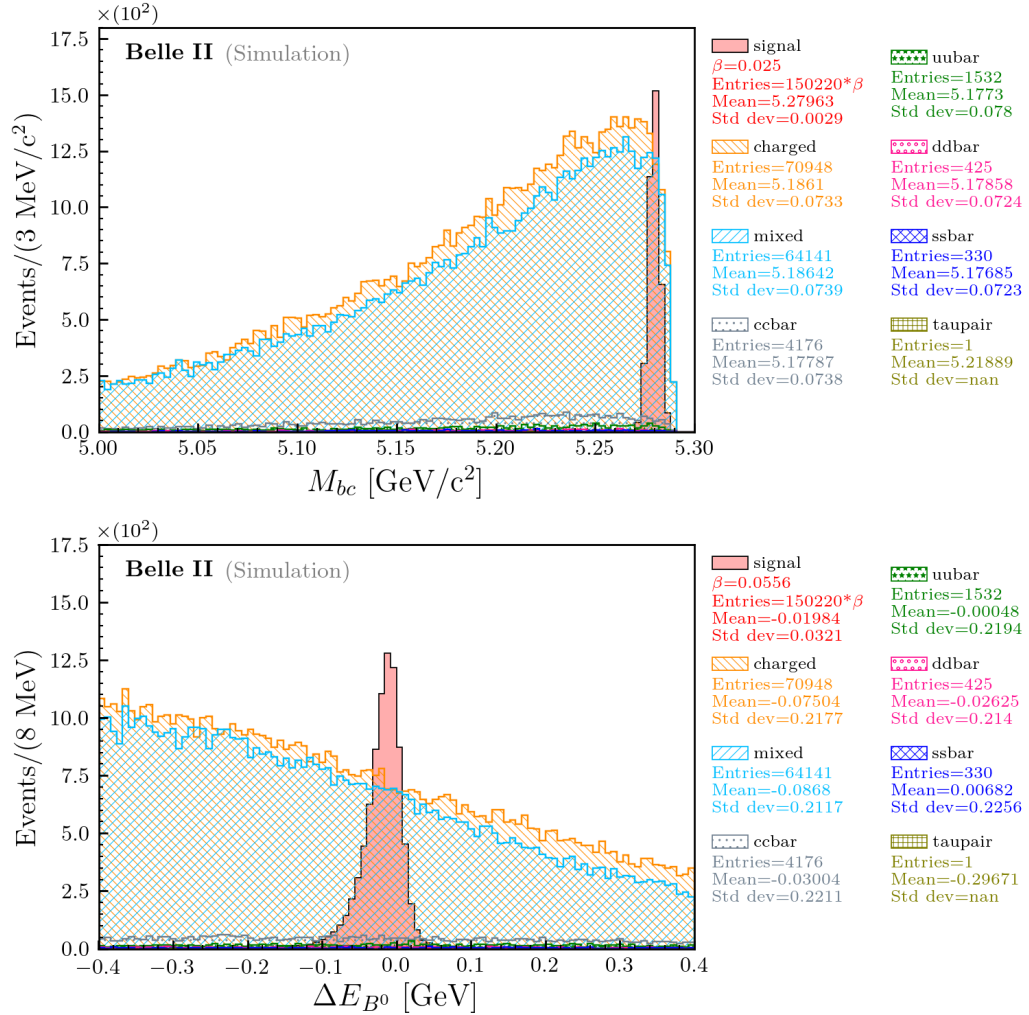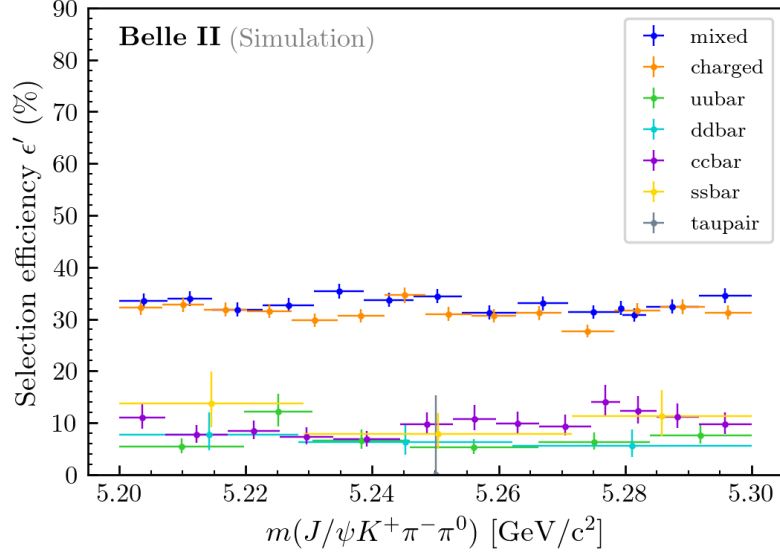
5.7. $m(J/\psi K^+\pi^-\pi^0)$ selection efficiency

The selection efficiency indicates us the number of events reconstructed that pass the optimized cuts N_{rec}^{sel} out of those reconstructed when only the pre-selection cuts are applied N_{rec}^{pre}. The momenta used for the reconstruction of the invariant masses in Figures 5-5 and 5-6 are those which we could experimentally reconstruct from footprints in detectors; hits and showers. The Monte Carlo simulation additionally provides the option of saving the *true momenta* for each particle; the momenta that are really generated by the generator and which do not have uncertainly from detector resolution. The advantage of using true momenta instead of reconstructed ones is that we remove resolution effects from the efficiency calculations. Thus, we can define the selection efficiency, as:

$$\epsilon'_{sel} := \frac{N_{rec}'^{sel}}{N_{rec}'^{pre}}, \tag{5-8}$$

where the single quote means that it was calculated using the true momenta. Figure 5-8 shows the selection efficiency ϵ'_{sel} of the invariant mass $m(J/\psi K^+\pi^-\pi^0)$ for each background type, where resonances produced by intermediate decay channels, shown in Table 5-2, are removed since they peak at $5.280\,\text{GeV/c}^2$. Misunderstood decay channels Ⓐ and Ⓑ (shown in Table 5-3) are not removed since we suspect that they do not certainly lead to the same 6-particle final state in the same side; combination with random particles becoming from the opposite side is made and, therefore, they could be typical background. Thus, when Ⓐ and Ⓑ are removed, a

little dip or hollow appears in mixed background around 5.280 GeV/c². On the other hand, it is expected that the overall shape of the selection efficiency ϵ'_{sel}, for each background sample, to be flat, such that the associated phase space to the $m(J/\psi K^+\pi^-\pi^0)$ distribution does not change significantly its shape after applying the optimization cuts. From Figure 5-8, different bin sizes for background samples and intervals were used since they have different number of entries. Thus, the size of each bin was chosen so that they have a similar number of entries. Clopper-Pearson statistical method was used to determine the selection efficiency (68% C.L.), where correlations among distributions used in the quotient (Eq. 5-8) are taken into account because the numerator is a subset of the denominator. It is desired and expected that ϵ'_{sel}, for backgrounds, decreases a lot when cuts on M_{bc} and ΔE_{B^0} variables be applied in future works. As an additional comment, the signal sample is not included in this analysis because all events are distributed at $\sim$ 5.280 GeV/c^2 and it does not make much sense to assign a bin to a single point.

5.8. $m(J/\psi\pi^-\pi^0)$ **resolution**

When people is selecting a TV to buy, they usually take care to choose those which have good resolution; a high pixel density equivalent to low pixel size. The same goal is sought by analysts in the particle physics area. Thus, it is important to know what is the minimum value that makes sense for the bin size in a specific distribution, which has to be related with its resolution. We are mainly interested in obtaining the resolution for the $m(J/\psi\pi^-\pi^0)$ variable. As previously mentioned, it is possible to obtain the invariant mass distribution from 4-momenta of particles and there are two types of simulated momenta; the true momenta *generated*, which reproduce exactly the decay of interest; and the momenta *reconstructed* from objects; hits and showers in detectors. The goal is to make that the reconstructed distribution $m(J/\psi\pi^-\pi^0)$ looks as similar as possible to the generated distribution. The difference between the reconstructed and generated distributions is referred as *Resolution* and four cases are studied (shown in Table 5-4), where little changes in the definition are applied.

Def.	Resolution (GeV/c^2)
1	$m(J/\psi\pi^-\pi^0)_{rec}$ - $m(J/\psi\pi^-\pi^0)_{gen}$
2	$m(J/\psi\pi^-\pi^0)_{rec}$ - $[m(\mu^+\mu^-)_{rec} - 3.09690\frac{GeV}{c^2}]$ - $m(J/\psi\pi^-\pi^0)_{gen}$
3	$m(J/\psi\pi^-\pi^0)_{rec}$ - $[m(\gamma\gamma)_{rec} - 0.13498\frac{GeV}{c^2}]$ - $m(J/\psi\pi^-\pi^0)_{gen}$
4	$m(J/\psi\pi^-\pi^0)_{rec}$ - $[(m(\gamma\gamma)_{rec} - 0.13498\frac{GeV}{c^2}) + (m(\mu^+\mu^-)_{rec} - 3.09690\frac{GeV}{c^2})]$ - $m(J/\psi\pi^-\pi^0)_{gen}$

Table 5-4.: Several definitions of mass resolution. Subscripts 'rec' and 'gen' for invariant masses refer to reconstructed and generated events.

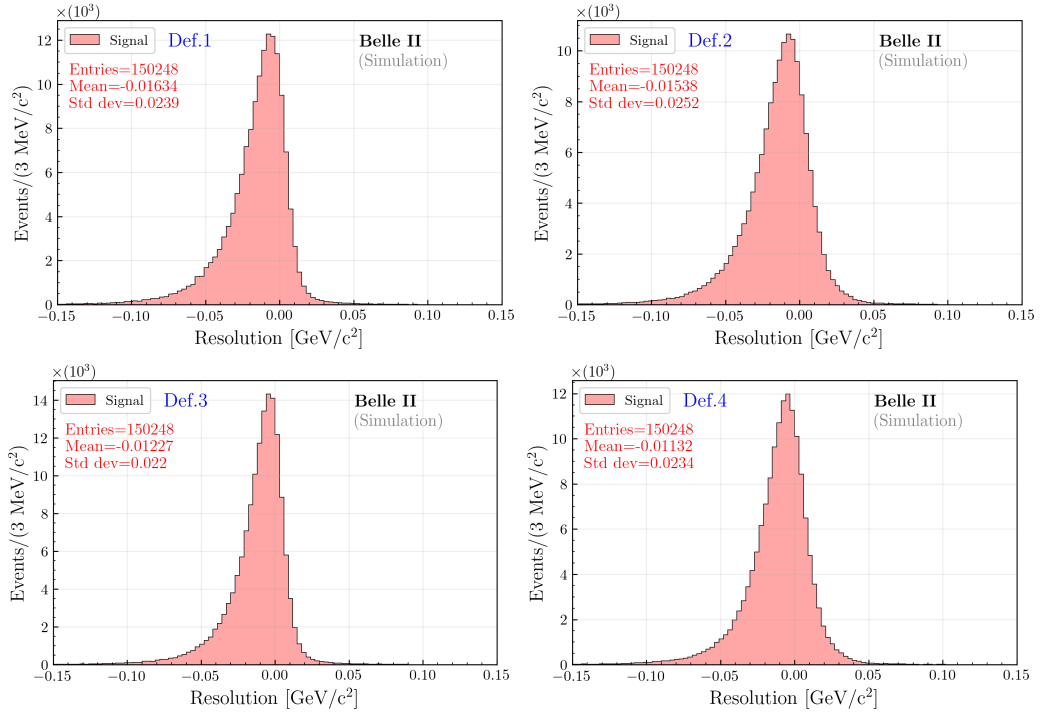**Figure 5-9**.: Resolution distribution for four different configurations in the complete detector acceptance ($17° \leq \theta_{comp.} \leq 150°$). Optimized requirements are already applied.

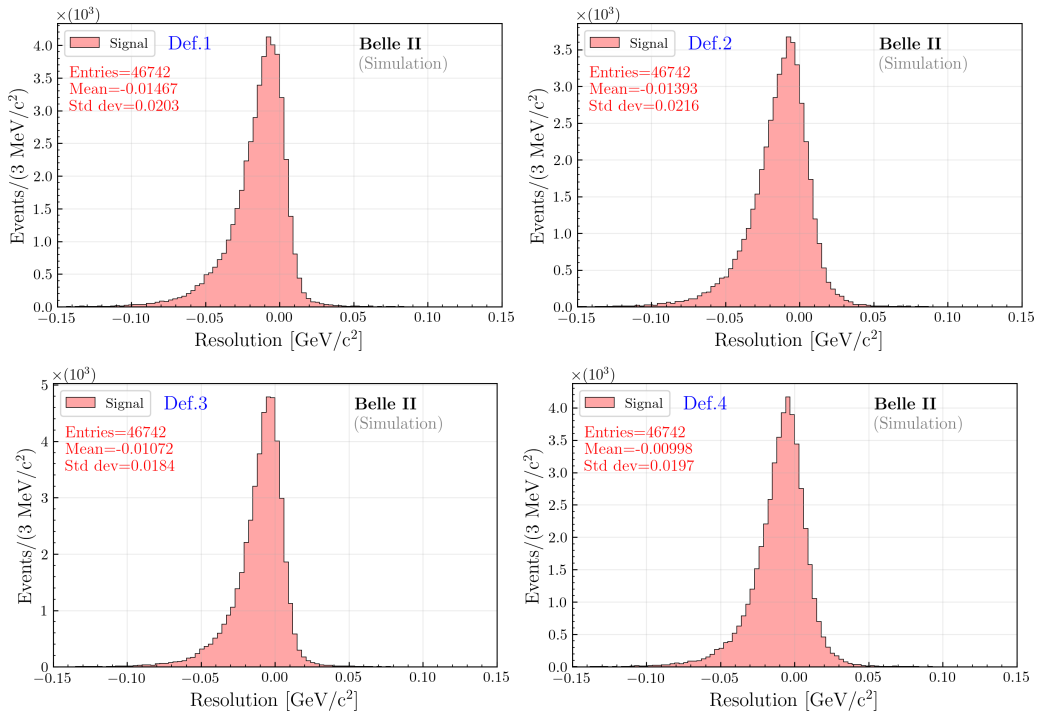**Figure 5-10**.: Resolution distribution for four different configurations only in the central or barrel region ($40° \leq \theta_{BRL} \leq 129°$). Optimized requirements are already applied.

The first definition is the traditional $m(J/\psi\pi^-\pi^0)_{rec}$ - $m(J/\psi\pi^-\pi^0)_{gen}$. The second and third definitions attempt to cancel, respectively, the effects of the resolution coming from the reconstruction of $m(\mu^+\mu^-)$ and $m(\gamma\gamma)$, and finally, the last definition tries to cancel both effects. The results are reported, in first case, for a polar angular amplitude $17° \le \theta_{comp.} \le 150°$ that covers the barrel (BRL), and forward (FWD) and backward (BWD) endcaps regions and, in the second case, only for events where particles decay in the barrel region $40° \le \theta_{BRL} \le 129°$. Results are shown in Figures 5-9 and 5-10.

As it is noted for the first case (see Fig. 5-9), the most narrow resolution distribution is obtained using the definition 3, where only the resolution cancellation $[m(\gamma\gamma)_{rec} - 0.13498 \text{ GeV}/c^2]$ is included; a standard deviation of $\sigma = 22 \text{ MeV}/c^2$ and a mean distribution value of -12.27 MeV/c^2 are obtained. Taking into account that the upper limit for the width resonance of $X(3872)$ is $\Gamma < 1.2 \text{ MeV}/c^2$, we realize that we need to reduce the values for the standard deviation (σ) in the resolution distributions to be able to observe narrower resonances, which could correspond to a possible exotic state. The fact that we have a wide distribution for resolution is mainly due to two causes: the first one is that low-energy photons from neutral pions produce an excess of data in the left zone in the $M_{\gamma\gamma}$ distribution (see top image in Fig. 5-2) that generates a shifting for the mean value respect to that reported by PDG ($\sim 0.13498 \text{ GeV}/c^2$). The second one is due to the Bremsstrahlung radiation emitted by muons, which causes energy losses and, therefore, the reconstruction of J/ψ particles from muons will be also accumulated to the left zone in the invariant mass distribution (see middle image in Fig. 5-2). On the other hand, a better mean value (closer to zero), but a higher σ, are obtained with definition 4, where both resolution cancellations are included. This improvement in the mean value of the resolution distribution (-11.32 MeV/c^2 with respect to -12.27 MeV/c^2, obtained in def.1) is given when the correction $[m(\mu\mu)_{rec} - 3.09690 \text{ GeV}/c^2]$ is included, because the mean value of the $(m_{\mu\mu})_{rec}$ distribution (3.09454 GeV/c^2) is closer to that reported by the PDG ($\sim 3.09690 \text{ GeV}/c^2$), in contrast to the mean value of $(m_{\gamma\gamma})_{rec}$ (131.32 MeV/c^2) to that reported by PDG ($\sim 134.98 \text{ MeV}/c^2$). However, the increase in the σ value in the resolution distribution when using def.4 is, likewise, due to the correction $[m(\mu\mu)_{rec} - 3.09690 \text{ GeV}/c^2]$, because σ is larger in $m(\mu\mu)_{rec}$ than in $m(\gamma\gamma)_{rec}$.

For case 2 (see Fig. 5-10), where polar angle amplitude is constrained only to θ_{BRL} (barrel zone), obtained results are similar to those of case 1; lowest standard deviation $\sigma = 18,4 \text{ MeV}/c^2$ with def.3 and the mean value closest to zero, -9.98 MeV/c^2 , with def.4. It is clear that obtained values in case 2 are better than those of case 1, but unfortunately the number of entries decreased to $\sim \frac{1}{3}$ from its initial value, which is unwanted when a exotic state is searched since only a few events are expected. It is important to highlight that although the obtained values for the statistical mean and σ are relatively large, they seem to be reasonable when we realize that the spectrum on which we are going to focus, $m(J/\psi\pi^-\pi^0)$, as well as any signal source

listed in Table 5-2, have widths of ~ 1.0 GeV/c^2, which is around 50 times larger than those obtained here for σ in the resolution distributions.

Finally, values of σ and statistical mean can be improved when alternative methods be used as Vertex or Mass Constraints, implemented in BASF2, where particles which come from the same father are restricted to be generated at the same point, or $\gamma\gamma$ and $\mu\mu$ candidates are forced to have an invariant mass equal to the π^0 and J/ψ mass, respectively. Additionally, the mean value can be improved when Bremsstrahlung corrections be applied to muons, where little missing energies are recovered. These methods are expected to be implemented in future works.

6. Data Analysis

As a preliminary study, in this section we show and compare distributions generated by a data sample of $\mathscr{L} = (8764.2 \pm 1.5)$ pb^{-1} (from the Exp. 7, 8 and 10, with data processing version Proc 11) and the simulated sample of $\mathscr{L} = 100$ fb^{-1} (from production MC13a), after applying the optimized cuts (listed in Table 5-1). A region in ΔE_{B^0} is selected such that 99.73% of signal is contained there. To achieve this, we developed an algorithm to count the number of signal events, starting from the mean value of ΔE_{B^0} and running symmetrically in both directions until cover that percentage. It was obtained that the region $\Theta = -0.212 < \Delta E_{B^0}[\text{GeV}] < 0.172$ contains that percentage of signal events.

Later, removal of events contained in Θ is applied on ΔE_{B^0} in order to blind (or exclude) the signal region, for both the simulated background sample (sum of generic contributions) and data, surviving only events distributed on the sidebands and a remaining 0.27% of signal. Figure 6-1 shows ΔE_{B^0} after Θ removal for both samples, keeping visible the complete signal distribution. The simulated background is scaled by the factor $\mathscr{L}^{Data}/\mathscr{L}^{MC} = 0.087642$ to get an equivalent integrated luminosity to data. Additionally, it is reminded that the β factor in plots only weights the signal to have similar height as the other distributions and, therefore, β does not have any physical meaning.
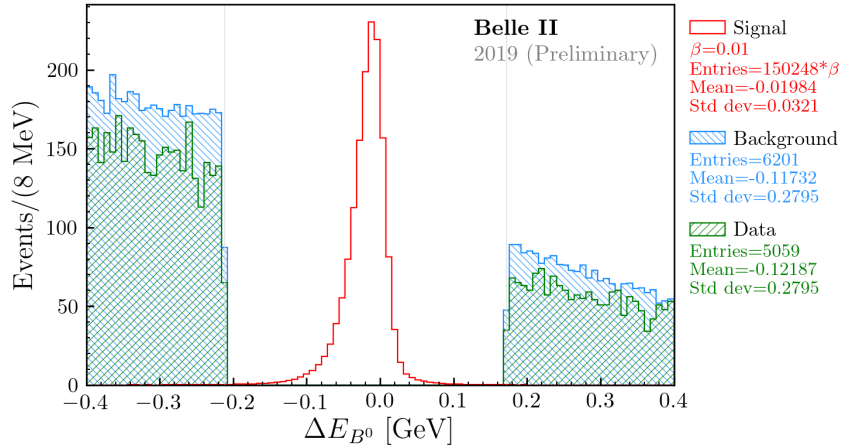
Figure 6-1.: Application of Θ removal (gray vertical lines) on the ΔE_{B^0} distribution, which remove 99.73% of the signal events. The optimized cuts (see Table 5-1) are already applied.
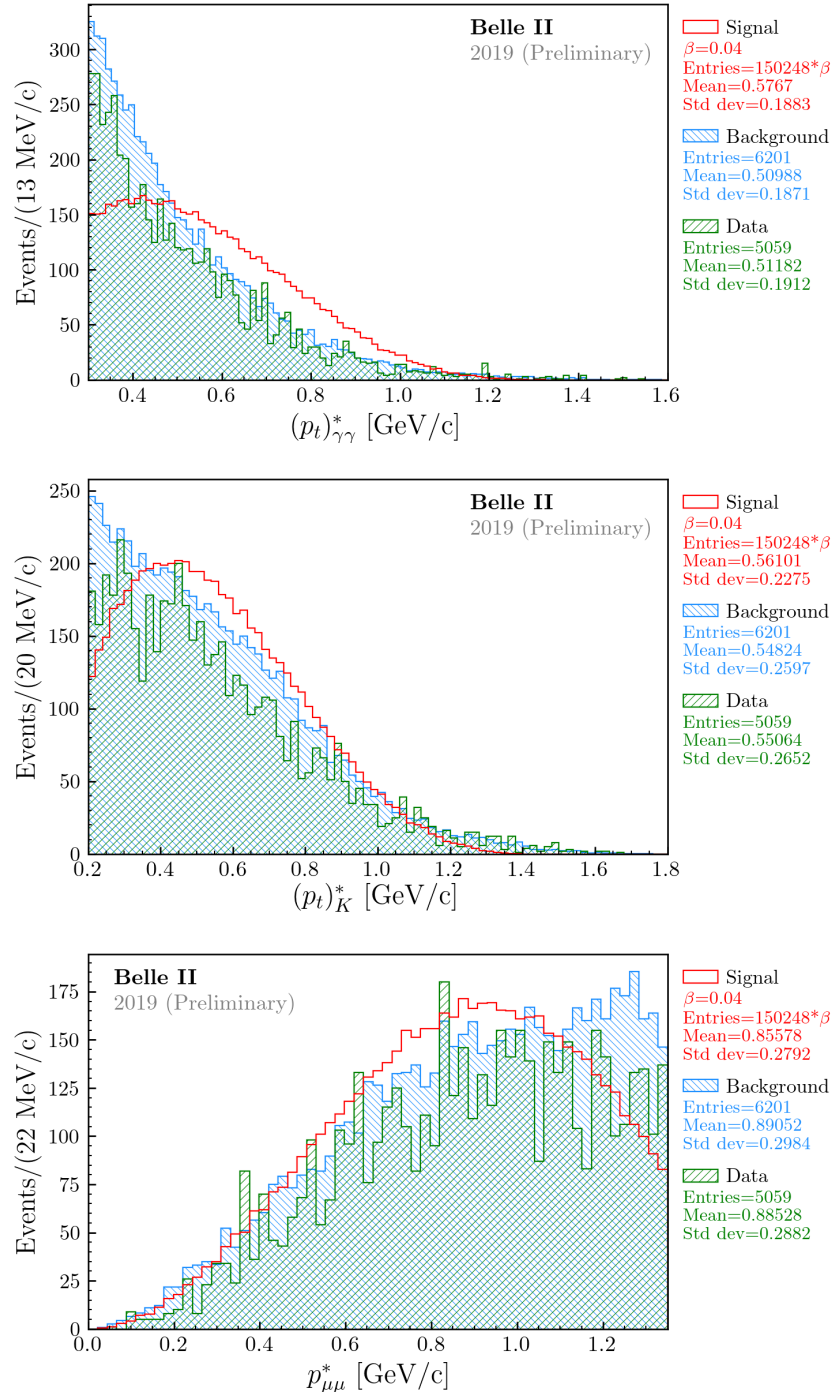
Figure 6-2.: Momenta distributions (measured in the CMS) after Θ removal and applying the optimization cuts (see Table 5-1). Shown are the transverse momentum of the di-photon (top) and charged kaons (middle) candidates and the total momentum for the di-muon candidate (bottom).
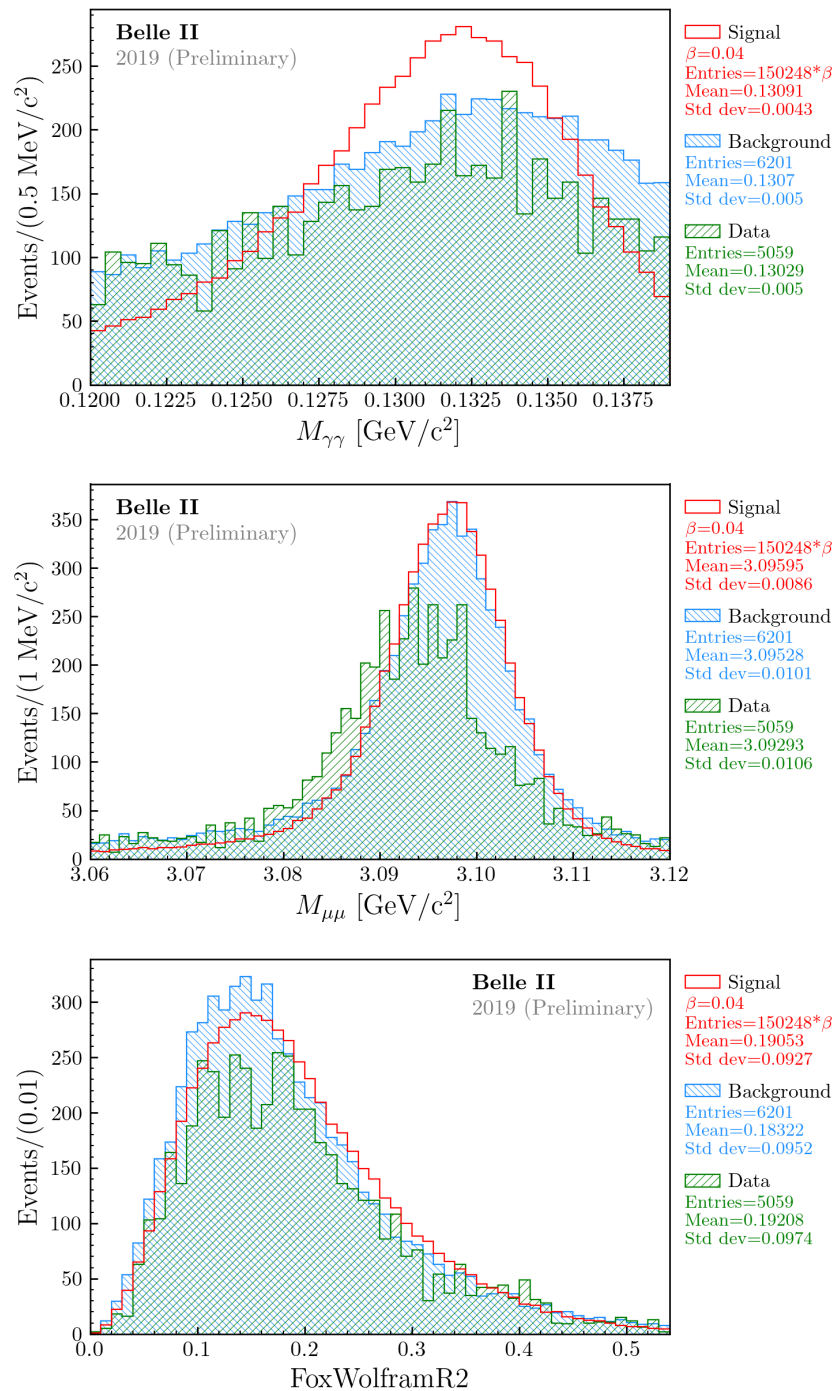
Figure 6-3.: Optimized cuts and Θ removal applied to mass distributions of reconstructed particles; di-photon (top) and di-muon (middle) candidates, and FoxWolframR2 (bottom), related with the event shape.
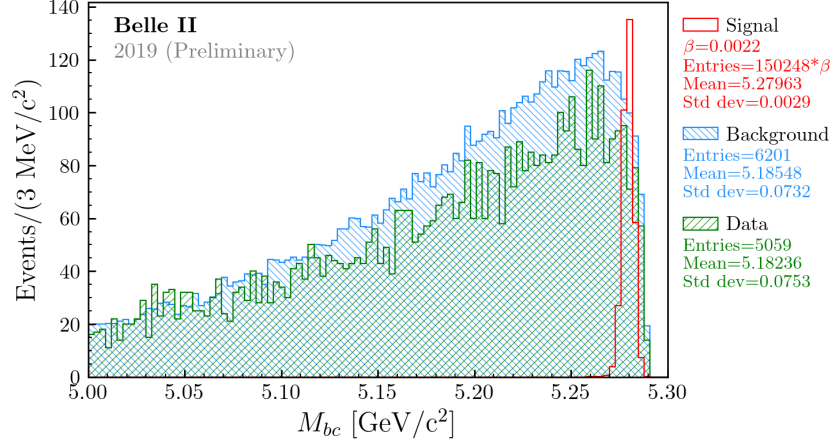
Figure 6-4.: Beam-energy constrained mass M_{bc} after Θ removal and applying the optimized cuts (see Table 5-1).

Any other variable could be chosen to cut the signal events, but the ΔE_{B^0} variable is preferred because its signal distribution is almost symmetric. Figures 6-2 to 6-4 show the distributions for the variables used in the selection (section 5.4), after Θ removal and applying the optimization cuts (shown in Table 5-1). As noted, the distribution for the simulated background sample is always higher than that for data, in each variable, despite of the first one is scaled by $\mathscr{L}^{Data}/\mathscr{L}^{MC}$. Fortunately, the shape of the distributions for both samples look alike, in such a way that it seems needed only an additional scale factor to match, except for $(p_t)_K^*$, around 0.25 GeV/c (see middle plot in Fig. 6-2), where it is shown that for data, this distribution seems to have a maximum value, in contrast with the simulated background sample, whose distribution seems to grow up indefinitely. With respect to the $p_{\mu\mu}^*$ variable (bottom plot in Fig. 6-2), it is not clear if around 1.3 GeV/c is happening the same situation as for $(p_t)_K^*$, since there is not enough statistic events in data, prevailing the statistical fluctuations. Unlike the previous variables, $M_{\mu\mu}$ (middle plot in Fig. 6-3) apparently presents a shifting in its the maximum value (statistical mode) between simulated events and data, which indicate us that the muons loose more energy (due to Bremsstrahlung radiation emission) than expected. These samples could get a better matching when Trigger corrections be applied in future works and improvements on MC simulations be done by developers.

The statistical significance, related with the traditional criterion for discovery [62], can be naively defined as:

$$significance := \frac{S}{\sqrt{B}}, \tag{6-1}$$

where S and B are respectively the number of signal and background entries observed inside a specific region (Θ region, for our case). The value for S is determined from the simulated events, where we found 508 entries corresponding to decays with intermediate resonances listed

in Table 5-2. Not all the distributions of these intermediate channels are completely contained within the Θ region, as shown in Appendix B, but just around $\sim 2/3$ of total events are. Additionally, these resulting signal events must be scaled to get the same integrated luminosity as data. Thus, for data, it is scarcely expected around $S \sim 508 \times 2/3 \times 0.087642 = 30$ signal events within the Θ region, for the integrated luminosity used so far.

It is possible to estimate the number of background events contained in the Θ region, for both the simulated sample and data, assuming that the shape of the distribution of ΔE_{B^0} behaves linearly in [-0.4, 0.4]. Figure 6-5 shows a linear approximation of the distribution shape for the simulated sample, where it is required that sidebands (blue regions) contain the 6201 entries. Thus, knowing the area of the sidebands and the area of the Θ region, it has been possible to obtain a estimated value for the number of background events in Θ, using a simple cross-multiplication. The same procedure is done for data, where it was required that its sidebands contain 5059 background events. The estimated results for background events in Θ region are $B_{MC} \sim 5800$ and $B_{Data} \sim 4900$, for the simulated sample and data, respectively. A more detailed calculation is shown in Appendix C.
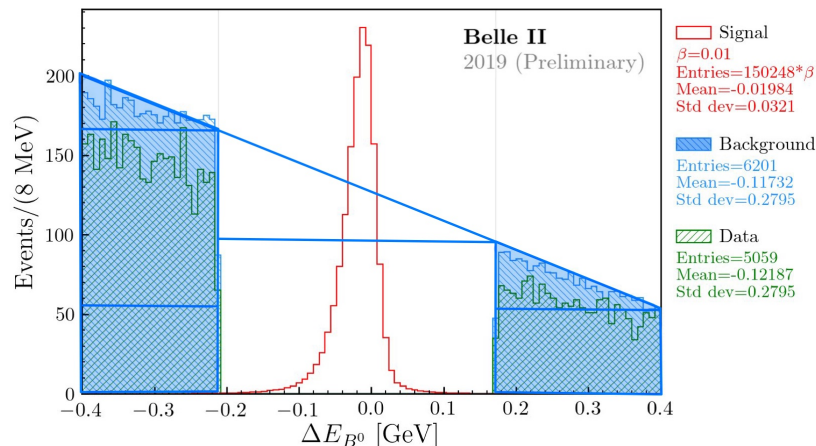
Figure 6-5.: Energy difference distribution ΔE_{B^0} after Θ removal and applying the optimized (see Table 5-1). Geometric figures (blue for sidebands) are superimposed to get an estimated value of the background entries, knowing their areas.

Estimated values for the significance (defined in Eq. 6-1) for the simulated sample and data are $\sim 0.39\sigma$ and $\sim 0.43\sigma$, respectively, where $S \sim 30$ was used for both of them. We report both significances due to data distributions do not match with the simulated ones (Trigger corrections have not been applied yet and Monte Carlo simulations are still being improved by developers). Thus, it seems reasonable to expect a significance into the interval $[0.39, 0.43]\sigma$, when data be analyzed in the Θ region. To obtain a significance larger than 5σ, it is needed to include a data sample with at least an integrated luminosity 13 times larger than it was used here, that is $\mathscr{L} \approx 114$ fb^{-1}, which could be obtained by the end of this year (2020).

7. Conclusions

In this work, we simulate and reconstruct the exclusive decay $B^0 \to K^+ J/\psi \pi^- \pi^0$, and a simulated generic background sample of 100 fb^{-1} was used to optimize our selection requirements. Optimized cuts, shown in Table 5-1, were determined by maximixing the FOM function (see Fig. 5-3) in such a way that signal events were well discriminated from the background ones, obtaining finally a total reconstruction efficiency of $\epsilon_T = 14.8\%$. On the other hand, we analyzed the invariant mass distribution $m(J/\psi \pi^- \pi^0)$ to study separately the found decays with intermediate resonances, as shown in Fig. 5-5, such that when exotic states be sought in future works, these are not confused with the new exotic resonances. Some of the decays with resonances found in this work, as radiative processes (listed in table 5-2), have not been previously considered by any experiment for a similar analysis. Misunderstood decays (apparently random combinations of signal and tag final states) were also studied in this analysis and listed in Table 5-3. Later, we plotted M_{bc} and ΔE_{B^0} variables (see Figures 5-4 and 5-7) that will be used in future 2D fits (or 3D fits if $m(J/\psi \pi^- \pi^0)$ is added) and for a definitive observation of the channel $B^0 \to K^+ J/\psi \pi^- \pi^0$ which will be a first step for an observation of any exotic state in the decay $X^- \to J/\psi \pi^- \pi^0$.

A study of selection efficiency on $m(K^+ J/\psi \pi^- \pi^0)$ distribution was made using the Clopper-Pearson statistical method (68% C.L.) and summarized in Fig. 5-8, where it was finally concluded that the optimization cuts do not change the shape associated to that distribution because resulting simulated backgrounds distribute flat-like. Additionally, we performed a resolution study, where the lowest standard deviation is obtained when we apply the resolution correction $[m(\gamma\gamma)_{rec} - 0.13498 \text{ GeV/c}^2]$ (Def.3 in Figures 5-9 and 5-10), and the mean value closest to zero is obtained when the resolution correction $[m(\mu^+\mu^-)_{rec} - 3.09690 \text{ GeV/c}^2]$ is applied (Def.4 in Figures 5-9 and 5-10). These values can be improved if we restrict the analysis to the polar angular amplitude only for detectors in the barrel (BRL) region; $40° \leq \theta_{BRL} \leq 129°$, but the number of entries decreases to $\sim \frac{1}{3}$ from its initial value, which is unwanted and, therefore, it is suggested to keep the window for both barrel and endcaps detectors.

Finally, a study is performed to compare the distributions (of variables used) between Monte Carlo simulations and data, using a data sample of $\mathscr{L} = (8764.2 \pm 1.5) \text{ pb}^{-1}$, where were applied the optimized cuts (see Table 5-1) and the blinding cut $-0.212 < \Delta E_{B^0}(\text{GeV/c}^2) < 0.172$, that removes the 99.73% of simulated signal events. It is found that the distributions obtained with

the simulated sample, after scaling, are higher than those with data, as shown in Figures 6-1 to 6-4, which suggests that Trigger corrections and/or improvements in MC simulations must be done. A estimated value for the significance is determined to be within $[0.39, 0.43]\sigma$, where the number of signal events are now obtained from the decays with intermediate resonances shown in Table 5-2. Finally, it is expected that the significance of 5σ be reached when a data sample of $\mathscr{L} \approx 114$ fb^{-1} be reached by Belle II.

8. Perspectives

An important progress was made in this work, which focuses on the search for charged exotic states in the $m(J/\psi\pi^-\pi^0)$ distribution. It is highlighted the observation of decays with intermediate resonances that have the same final state, listed in Table 5-2. When they are excluded, it is observed that peaks on M_{bc} and ΔE_{B^0} are practically eliminated (compare Figures 5-4 and 5-7), but unfortunately a little structure remained, meaning that in future works we expect to find additional intermediate resonances that we must take into account (or veto) on M_{bc}, ΔE_{B^0} and $m(J/\psi\pi^-\pi^0)$ in a 3D fit. Of course, it will be needed to classify correctly the decays with intermediate resonances found in this work (specially the misunderstood ones, which are listed in Table 5-3) and those that we can find later. To get a right classification, some changes on codes of the Belle II software will need to be made, in order to obtain more information about relationship among particles and its complete decay chain for both signal and tag side.

To get more statistical data (signal events), we can include the $J/\psi \to e^+e^-$ final state, where new techniques must be learned and employed due to electrons usually emit more Bremsstrahlung radiation than muons and, therefore, energy corrections have to be included. Additional decays can be added in the analysis, as $B^- \to K_S^0 X^-$, $X^- \to J/\psi\pi^-\pi^0$, $K_S^0 \to \pi^+\pi^-$, to get more signal events. On the other hand, other interesting variables (as the vertex probability and constrained masses) and requirements on them will be considered to obtain better discrimination of signal from background events and, later, to obtain more pure results for any observed charged exotic state in real data. Furthermore, many performance studies and crosschecks are expected to be implemented to ensure that future results are reliable. Finally, we expect additional data this year to observe promptly any signal distribution with a significance larger than 5σ.

A. Swapped candidates

When BASF2 attaches the information contained in the ReconstructDecay file to reconstruct the decay channel of interest from the tracks, it additionally tests all possible track combinations and values for electric charges, and only keep those events that satisfy the (pre-selection) cuts established in the ReconstructDecay file. Thus, it is possible to reconstruct a fake decay chain where two particles are reconstructed with the wrong mass assignments. This is the case for the charged K and π in the decay $B^0 \to K^+ J/\psi \pi^- \pi^0$, where in addition to the true decay, it has been reconstructed a wrong decay where K/π masses are exchanged. To identify and select these events, the mcPDG variables are needed, which give the PDG number of the particle used, requiring that $\text{abs}(\text{mcPDG}(K)) = 211$, $\text{abs}(\text{mcPDG}(K)) = 321$ and $\text{mcPDG}(K) \times \text{mcPDG}(\pi) = -211 \times 321$, where their PDG numbers have been exchanged and their electric charges are required to have opposite signs. Right PDG numbers are used for the other particles to be sure that we are selecting only these swapped candidates. When all pre-selection cuts are applied, except kaonID>0.1 and pionID>0.1, the swap events projected on the M_{bc} variable are distributed as shown on the left in Figure A-1, and later, on the right, are shown the remaining swapped events after applying these soft ID cuts; kaonID>0.1 and pionID>0.1.
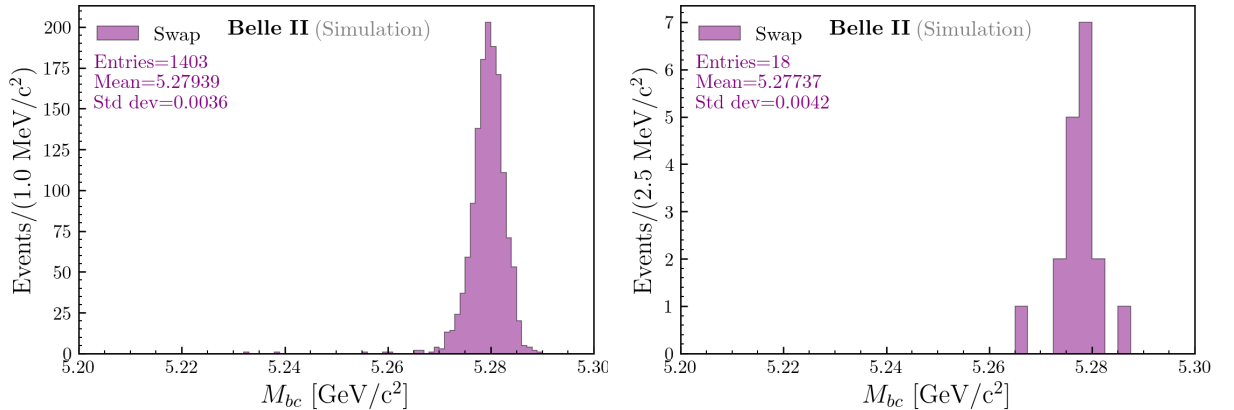

Figure A-1.: Distribution for the swapped events projected on M_{bc}, for charged K and π before (left) and after (right) applying the kaonID>0.1 and pionID>0.1 cuts.

The 98.7% of these swapped events are removed, while true decays are reduced 18.9%, as shown in Fig. A-2, where the higher (red) and lower (green) distributions correspond to the signal events

projected on M_{bc}, before and after applying these soft ID cuts, respectively. As comment, for this swap study we use a sample with only 10^4 simulated events, to show why it is needed to use the kaonID and pionID variables.

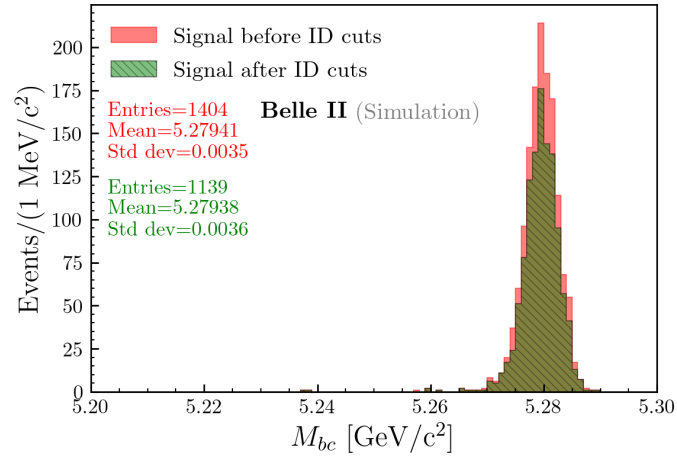**Figure A-2**.: Distribution for the true signal decays projected on M_{bc}, before (higher, in red) and after (lower, in green) applying the kaonID>0.1 and pionID>0.1 cuts.

B. M_{bc} and ΔE_{B^0} distributions for the intermediate decay channels
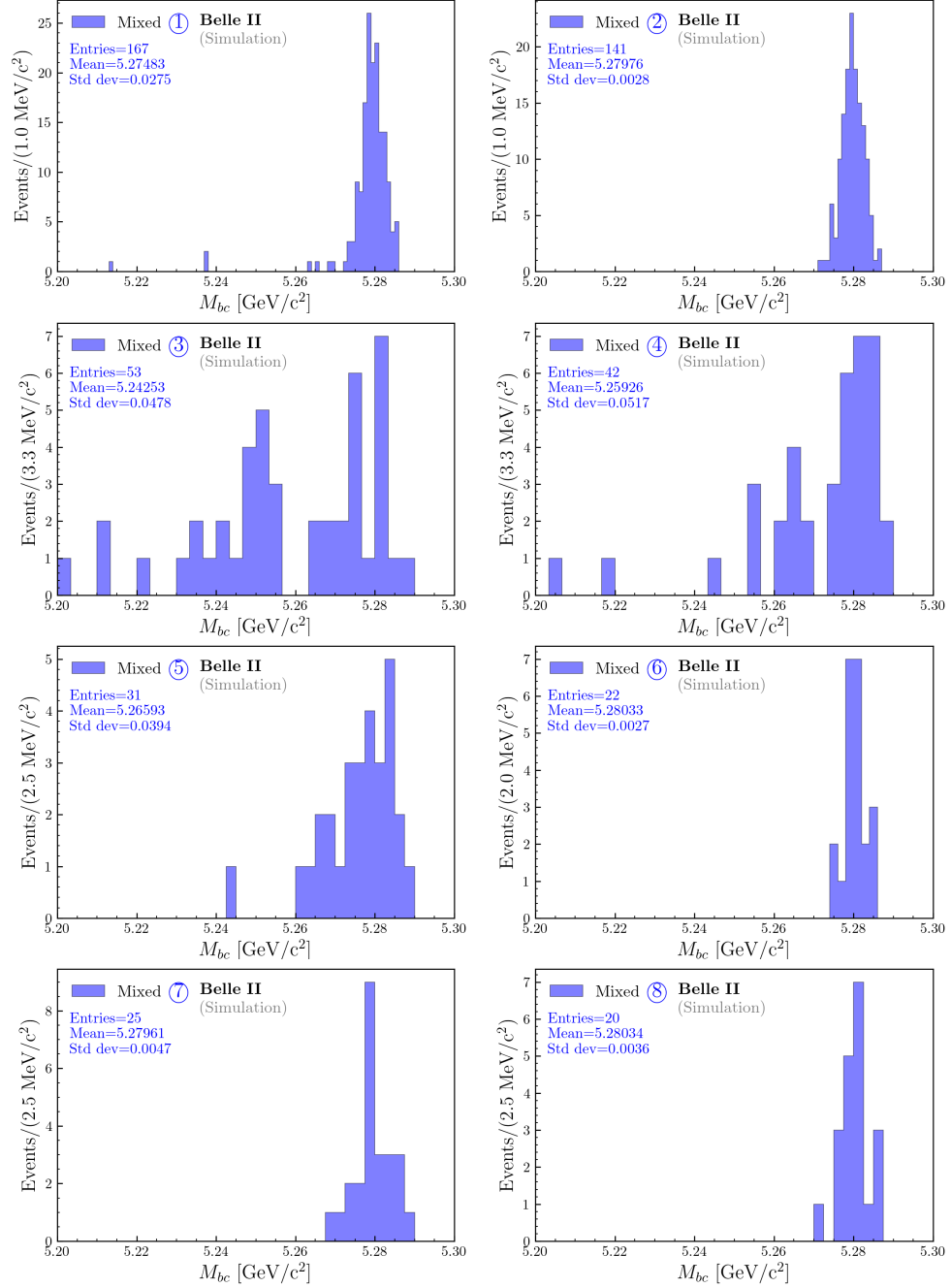

Figure B-1.: Distribution for the decay channels with intermediate resonances ①-⑧ (listed in Table 5-2) on M_{bc}. Optimized cuts (see Table 5-1) are already applied.
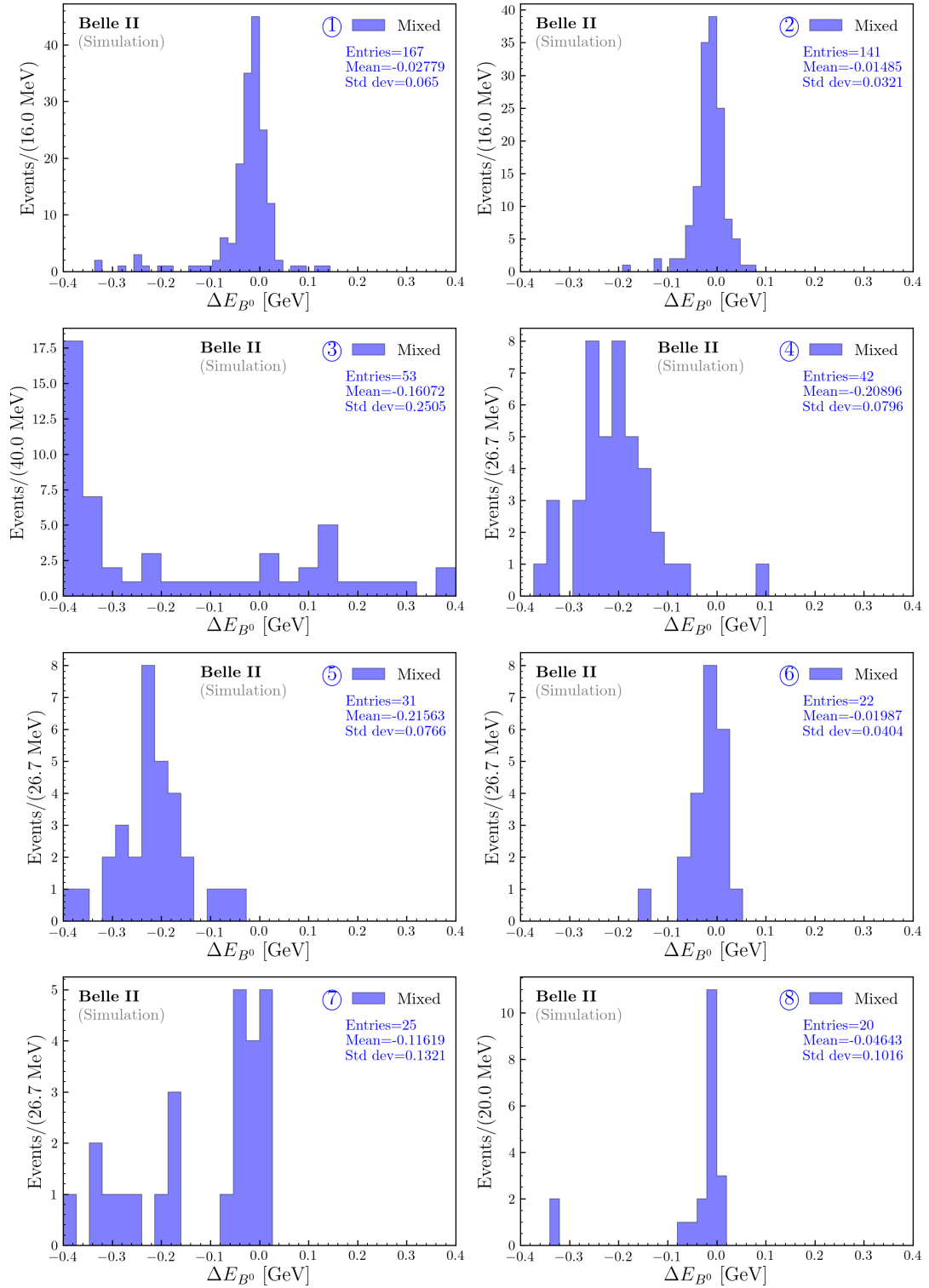
Figure B-2.: Distribution for the decay channels with intermediate resonances ①-⑧ (listed in Table 5-2) on ΔE_{B^0}. Optimized cuts (see Table 5-1) are already applied.
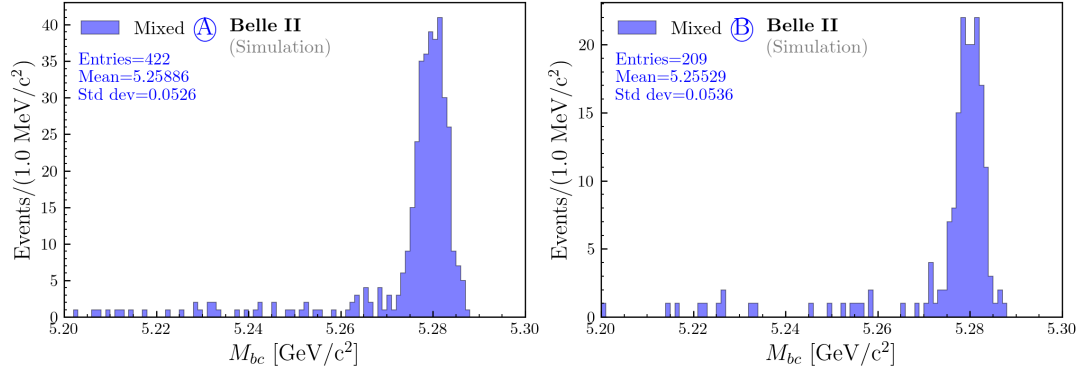
Figure B-3.: Distribution for the misunderstood decays with intermediate resonances Ⓐ and Ⓑ (listed in Table 5-3) on M_{bc}. Optimized cuts (see Table 5-1) are already applied.
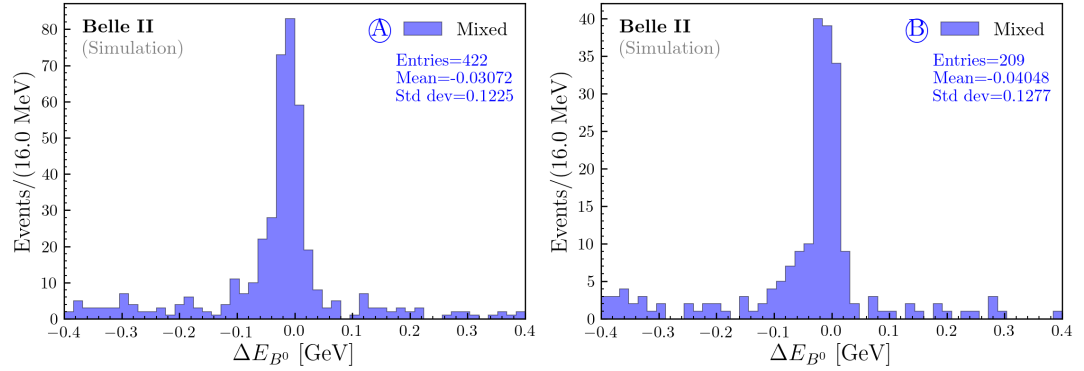

Figure B-4.: Distribution for the misunderstood decays with intermediate resonances Ⓐ and Ⓑ (listed in Table 5-3) on ΔE_{B^0}. Optimized cuts (see Table 5-1) are already applied.

As noted from Fig. B-1, the intermediate resonances ①-⑧ distribute around ~ 5.280 GeV/c², highlighting that ③ present a tail due to the radiative processes (photon emissions). From Fig. B-2, the resonances ③, ④ and ⑤ are distributed in outer regions from 0 GeV, which is a good sign because a soft cut on ΔE_{B^0} (eg.: abs(ΔE_{B^0})< 0.1 GeV) easily can remove (almost completely) these decays with intermediate resonances. Unfortunately, the misunderstood resonances Ⓐ and Ⓑ, distributed on M_{bc} and ΔE_{B^0} in Figures B-3 and B-4, respectively, show that no obvious cut can be applied to remove them without disturbing the signal, which is distributed in the same region. It is needed further studies to make sure what is the origin of these decays. In particular, we need to improve the MC matching to identify the complete decay chain for both signal and tag sides.

C. A more detailed calculation for the estimation of background events in the blinded region

The area of sidebands become approximate using simple geometric figures; triangles and rectangles, generated once a line segment is drawn upon the distribution. These line segments used are not obtained from any linear fit. Additionally, it is omitted the use of units (GeV), for simplicity.

For the area calculation of the sideband $\boxed{1}$ for the simulated Monte Carlo background (see in Fig. C-1), we simply sum the area of the rectangle and the triangle as: $A_\square = 0.188 \times 165$, $A_\triangle = \frac{1}{2} \times 0.188 \times (200 - 165)$, obtaining $A_1 = A_\square + A_\triangle = 34.31$, where $0.188 = |-0.4 - (0.212)|$ is the base width for the sideband $\boxed{1}$. Analogously, it can be easily obtained $A_2 = 17.1$ and $A_3 = 49.92$. As the area $A_1 + A_2 = 51.41$ is required to have 6021 background events, then, with a simple cross-multiplication, it is obtained that A_3 must have around 5847 events (~ 5800). Performing a similar process for Data background and using the values shown on the plot in Fig. C-2, it is obtained that $A_1 + A_2 = 40.47$ and $A_3 = 39.36$. As $A_1 + A_2$ is required to have 5059 events, it is obtained, again using a cross-multiplication, that A_3 must have around 4920 background events (~ 4900).
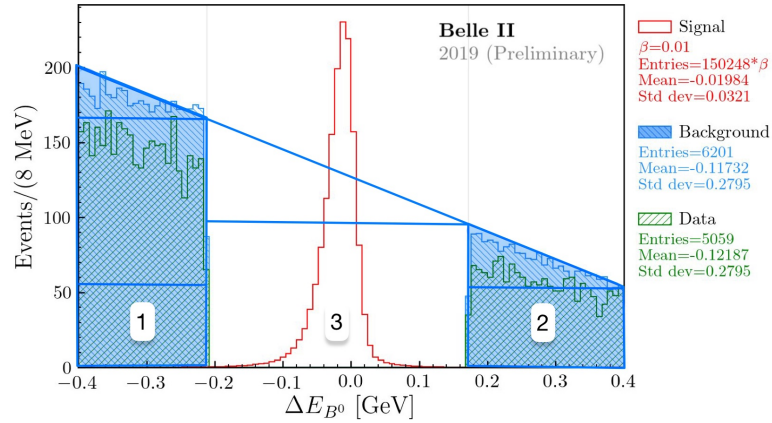
Figure C-1.: Energy difference distribution ΔE_{B^0} used for the estimated area calculations of sidebands $\boxed{1}$ and $\boxed{2}$ for the simulated Monte Carlo Background on this variable. Optimized cuts (see Table 5-1) and Θ removal are already applied.

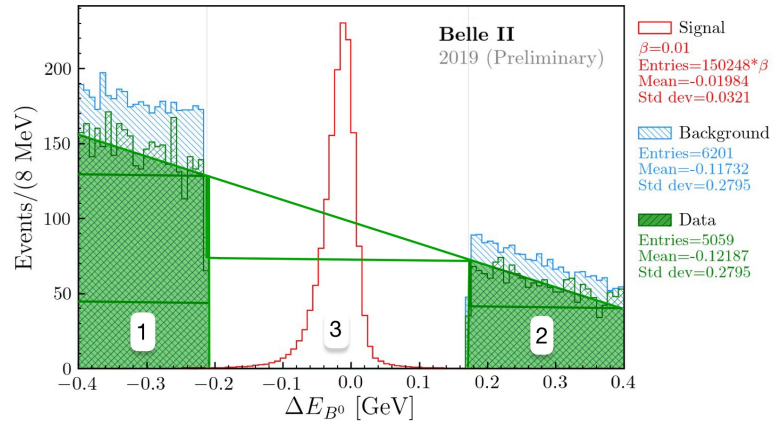**Figure C-2**.: Energy difference distribution ΔE_{B^0} used for the estimated area calculations of sidebands $\boxed{1}$ and $\boxed{2}$ of Data on this variable. Optimized cuts (see Table 5-1) and Θ removal are already applied.

Bibliography

[1] Wikipedia. Stardard model of elementary particles and gravity. URL: https://en.wikipedia. org/wiki/Physics_beyond_the_Standard_Model.

[2] Particle Data Group. $B^0 - \bar{B}^0$ Mixing. URL: https://pdg.lbl.gov/2019/reviews/rpp2018-rev-b-bar-mixing.pdf.

[3] Nora Brambilla, Simon Eidelman, Christoph Hanhart, Alexey Nefediev, Cheng-Ping Shen, Christopher E Thomas, Antonio Vairo, and Chang-Zheng Yuan. The XYZ states: experimental and theoretical status and perspectives. *Physics Reports*, 2020.

[4] Belle II Web Page. SuperKEKB accelerator. URL: https://www.kek.jp/en/newsroom/20 18/03/22/0900/.

[5] Abi Soffer. Belle II: status and prospects. URL: https://docs.belle2.org/record/1152/files /belle2-talk-conf-2018-119.pdf.

[6] The Belle II Collaboration. Full detector Belle II. URL: https://confluence.desy.de/down load/attachments/35009238/BelleII_Slide.pdf.

[7] Peter Kodyš, F Abudinen, K Ackermann, P Ahlburg, H Aihara, M Albalawi, O Alonso, L Andricek, R Ayad, T Aziz, et al. The Belle II Vertex Detector integration. *Nuclear Instruments and Methods in Physics Research Section A: Accelerators, Spectrometers, Detectors and Associated Equipment*, 936:616–620, 2019.

[8] I Adachi, TE Browder, P Križan, S Tanaka, Y Ushiroda, Belle II Collaboration, et al. Detectors for extreme luminosity: Belle ii. *Nuclear Instruments and Methods in Physics Research Section A: Accelerators, Spectrometers, Detectors and Associated Equipment*, 907:46–59, 2018.

[9] Steven Robertson. Belle II Collaboration. Belle II: status and prospects. URL: https://indico.tlabs.ac.za/event/75/contributions/1161/attachments/498/542/BelleII_ robertsonv2.pdf.

[10] Choongjae Yoon. Time-of-propagation counter for the leps. *IEEE Trans.Nucl.Sci. 61 (2014) 2601-2607*, 61:2601, 08 2014.

[11] S. Iwata, I. Adachi, Koji Hara, T. Iijima, Hirokazu Ikeda, H. Kakuno, Hiroki Kawai, Teruki Kawasaki, S. Korpar, Peter Krizan, T. Kumita, S. Nishida, Seishi Ogawa, R. Pestotnik, L. Å antelj, Andrej Seljak, T. Sumiyoshi, Makoto Tabata, Elvedin Tahirovic, and Yosuke Yusa. Particle identification performance of the prototype aerogel rich counter for the Belle II experiment. *Progress of Theoretical and Experimental Physics*, 2016:033H01, 03 2016.

[12] Belle II Collaboration. Belle II technical design report.kek report 2010-1,version 1.5, october 2010.

[13] Confluence. Software basf2 introduction. URL: https://confluence.desy.de/display/BI/Soft--ware+Basf2Introduction.

[14] Emi Kou, Phillip Urquijo, W Altmannshofer, F Beaujean, G Bell, M Beneke, II Bigi, F Bishara, M Blanke, C Bobeth, et al. The Belle II physics book. *Progress of Theoretical and Experimental Physics*, 2019(12):123C01, 2019.

[15] S-K Choi, SL Olsen, K Abe, T Abe, I Adachi, Byoung Sup Ahn, H Aihara, K Akai, M Akatsu, M Akemoto, et al. Observation of a narrow charmoniumlike state in exclusive $B^{\pm} \to K^{\pm}\pi^+\pi^- J/\psi$ decays. *Physical review letters*, 91(26):262001, 2003.

[16] Darin Acosta, T Affolder, MH Ahn, T Akimoto, MG Albrow, D Ambrose, S Amerio, D Amidei, A Anastassov, K Anikeev, et al. Observation of the narrow state $X(3872) \to J/\psi\pi^+\pi^-$ in pp collisions at $\sqrt{s} = 1.96$ TeV. *Physical review letters*, 93(7):072001, 2004.

[17] R. Aaij, C. Abellan Beteta, B. Adeva, M. Adinolfi, C. Adrover, A. Affolder, Z. Ajaltouni, J. Albrecht, F. Alessio, M. Alexander, and et al. Determination of the X(3872) meson quantum numbers. *Physical Review Letters*, 110(22), May 2013.

[18] M. Ablikim, M. N. Achasov, X. C. Ai, O. Albayrak, M. Albrecht, D. J. Ambrose, and collaborators. Observation of $Z_c(3900)^0$ in $e^+e^- \to \pi^0\pi^0 J/\psi$. *Phys. Rev. Lett.*, 115:112003, Sep 2015.

[19] S.-K. Choi, S. L. Olsen, I. Adachi, H. Aihara, and collaborators. Observation of a resonance-like structure in the $\pi^{\pm}\psi'$ mass distribution in exclusive $B \to K\pi^{\pm}\psi'$ decays. *Phys. Rev. Lett.*, 100:142001, Apr 2008.

[20] Roel Aaij et al. Observation of $J/\psi p^+$ Resonances Consistent with Pentaquark States in $\Lambda_b^0 \to J/\psi K^- p^+$ Decays. *Phys. Rev. Lett.*, 115:072001, 2015.

[21] Peter W. Higgs. Broken symmetries and the masses of gauge bosons. *Phys. Rev. Lett.*, 13:508–509, Oct 1964.

[22] H.G. Moser. Evidence for B0 anti-B0 oscillations at UA1. In *International Europhysics Conference on High-energy Physics*, pages 363–364, 6 1987.

[23] H. Schroder. Observation of B0 anti-B0 oscillations. In *International Europhysics Confer-ence on High-energy Physics*, pages 365–367, 1987.

[24] A. Abulencia, J. Adelman, T. Affolder, T. Akimoto, M. G. Albrow, D. Ambrose, S. Amerio, D. Amidei, A. Anastassov, K. Anikeev, and et al. Observation of B_s-$\bar{B}_s$ oscillations. *Physical Review Letters*, 97(24), Dec 2006.

[25] Particle Data Group. B0. URL: https://pdg.lbl.gov/2018/listings/rpp2018-list-B-zero.pdf.

[26] Murray Gell-Mann. A Schematic Model of Baryons and Mesons. *Phys. Lett.*, 8:214–215, 1964.

[27] Bryan R Webber. A qcd model for jet fragmentation including soft gluon interference. *Nuclear Physics B*, 238(3):492–528, 1984.

[28] Ahmed Ali, Luciano Maiani, and Antonio D Polosa. *Multiquark hadrons.* Cambridge University Press, 2019.

[29] Roel Aaij, Diego Torres Machado, Matthew John Bradley, Gregory Ciezarek, Maciej Woj-ciech Dudek, Paula Collins, Steffen Georg Weber, Wenbin Qian, Halime Sazak, Achim Voll-hardt, et al. arXiv: A model-independent study of resonant structure in $B^+ \rightarrow D^+D^-K^+$ decays. Technical report, 2020.

[30] Roel Aaij, C Abellán Beteta, Thomas Ackernley, Bernardo Adeva, Marco Adinolfi, Hossein Afsharnia, Christine Angela Aidala, Salvatore Aiola, Ziad Ajaltouni, Simon Akar, et al. Observation of structure in the J/ψ-pair mass spectrum. *arXiv preprint arXiv:2006.16957*, 2020.

[31] VM Abazov, B Abbott, M Abolins, BS Acharya, DL Adams, M Adams, T Adams, M Agelou, J-L Agram, SN Ahmed, et al. Observation and properties of the X(3872) decay-ing to $J/\psi\pi^+\pi^-$ in pp collisions at $\sqrt{s} = 1.96$ TeV. *Physical review letters*, 93(16):162002, 2004.

[32] Bernard Aubert, R Barate, D Boutigny, F Couderc, J-M Gaillard, A Hicheur, Y Karyotakis, JP Lees, V Tisserand, A Zghiche, et al. Study of the $B^- \rightarrow J/\psi K^-\pi^+\pi^-$ decay and mea-surement of the $B^- \rightarrow X(3872)K^-$ branching fraction. *Physical Review D*, 71(7):071103, 2005.

[33] Particle Data Group. X(3872). URL: https://pdg.lbl.gov/encoder_listings/m176.pdf.

[34] S.-K. Choi, S. L. Olsen, K. Trabelsi, I. Adachi, H. Aihara, K. Arinstein, D. M. Asner, T. Aushev, A. M. Bakich, E. Barberio, and et al. Bounds on the width, mass difference and other properties of $X(3872) \rightarrow \pi^+\pi^- J/\psi$ decays. *Physical Review D*, 84(5), Sep 2011.

[35] Angelo Esposito, Elena G. Ferreiro, Alessandro Pilloni, Antonio D. Polosa, and Carlos A. Salgado. The nature of $X(3872)$ from high-multiplicity pp collisions, 2020.

[36] Zhi-Gang Wang. Analysis of the Z(4430) as the first radial excitation of the Zc(3900). *Communications in Theoretical Physics*, 63(3):325–330, mar 2015.

[37] Particle Data Group. $Z_c(3900)$. URL: https://pdg.lbl.gov/2019/listings/rpp2019-list-Z-c-3900.pdf.

[38] M. Ablikim, M. N. Achasov, X. C. Ai, O. Albayrak, M. Albrecht, D. J. Ambrose, and collaborators. Observation of a neutral structure near the $D\bar{D}^*$ mass threshold in $e^+e^- \to (D\bar{D}^*)^0\pi^0$ at $\sqrt{s} = 4.226$ and 4.257 GeV. *Phys. Rev. Lett.*, 115:222002, Nov 2015.

[39] M. Ablikim, M.N Achasov, P. Adlarson, S. Ahmed, Malte Albrecht, Antonio Amoroso, and collaborators. Study of the process $e^+e^- \to \pi^0\pi^0 J/\psi$ and neutral charmonium-like state $Z_c(3900)^0$. *Physical Review D*, 102, 07 2020.

[40] B. Aubert, R. Barate, D. Boutigny, F. Couderc, Y. Karyotakis, J. P. Lees, V. Poireau, V. Tisserand, A. Zghiche, E. Grauges, and et al. Observation of a broad structure in the $\pi^+\pi^- J/\psi$ mass spectrum around 4.26 GeV/c^2. *Physical Review Letters*, 95(14), Sep 2005.

[41] Q. He, J. Insler, H. Muramatsu, C. S. Park, E. H. Thorndike, F. Yang, and collaborators. Confirmation of the $Y(4260)$ resonance production in initial state radiation. *Phys. Rev. D*, 74:091104, Nov 2006.

[42] C. Z. Yuan, C. P. Shen, P. Wang, S. McOnie, I. Adachi, H. Aihara, V. Aulchenko, T. Aushev, S. Bahinipati, V. Balagura, and collaborators. Measurement of the $e^+e^- \to \pi^+\pi^- J/\psi$ cross section via initial-state radiation at Belle. *Phys. Rev. Lett.*, 99:182004, Nov 2007.

[43] M. Ablikim, M. N. Achasov, S. Ahmed, X. C. Ai, O. Albayrak, M. Albrecht, and collaborators. Precise measurement of the $e^+e^- \to \pi^+\pi^- J/\psi$ Cross Section at Center-of-Mass Energies from 3.77 to 4.60 GeV. *Phys. Rev. Lett.*, 118:092001, Mar 2017.

[44] Particle Data Group. $Y_c(4260)$. URL: https://journals.aps.org/prd/pdf/10.1103/PhysRev D.98.030001.

[45] Ting-Wai Chiu and Tung-Han Hsieh. $Y(4260)$ on the lattice. *Phys. Rev. D*, 73:094510, May 2006.

[46] Yun-Hua Chen, Ling-Yun Dai, Feng-Kun Guo, and Bastian Kubis. Nature of the $Y(4260)$: A light-quark perspective. *Phys. Rev. D*, 99:074016, Apr 2019.

[47] R. Aaij, B. Adeva, M. Adinolfi, A. Affolder, Z. Ajaltouni, J. Albrecht, F. Alessio, M. Alexander, S. Ali, G. Alkhazov, and et al. Observation of the resonant character of the Z(4430) state. *Physical Review Letters*, 112(22), Jun 2014.

[48] Particle Data Group. $Z_c(4430)$. URL: https://pdg.lbl.gov/2018/listings/rpp2018-list-Z-c-4430.pdf.

[49] Fabian Goerke, Thomas Gutsche, Mikhail A. Ivanov, Jürgen G. Körner, Valery E. Lyubovit-skij, and Pietro Santorelli. Four-quark structure of the Zc(3900), Z(4430) and Xb(5568) states. *Physical Review D*, 94(9), Nov 2016.

[50] Kazunori Akai, Kazuro Furukawa, and Haruyo Koiso. SuperKEKB collider. *Nuclear Instruments and Methods in Physics Research Section A: Accelerators, Spectrometers, Detectors and Associated Equipment*, 907:188–199, Nov 2018.

[51] Belle II experiment collaborators. SuperKEKB collider achieves the world's highest luminosity. URL:https://www.kek.jp/en/newsroom/2020/06/26/1400/. Jun 2020.

[52] C Milardi, M A Preger, P Raimondi, and F Sgamma. High luminosity interaction region design for collisions inside high field detector solenoid. *Journal of Instrumentation*, 7(03), Mar 2012.

[53] B. Paschen, F. Abudinen, K. Ackermann, and collaborators. Belle II Pixel Detector: Performance of final DEPFET modules. *Nuclear Instruments and Methods in Physics Research Section A: Accelerators, Spectrometers, Detectors and Associated Equipment*, 958:162222, 2020. Proceedings of the Vienna Conference on Instrumentation 2019.

[54] E Barberio, T Baroncelli, G Caria, GN Taylor, P Urquijo, J Webb, S Williams, A Bauer, F Buchsteiner, M Friedl, et al. Performance studies of Belle II Silicon Vertex Detector. In *Proceedings of Science*, 2018.

[55] E Torassa et al. Particle identification with the TOP and ARICH detectors at Belle II. *Nuclear Instruments and Methods in Physics Research Section A: Accelerators, Spectrometers, Detectors and Associated Equipment*, 824:152–155, 2016.

[56] S. Sandilya. Particle identification with the TOP and ARICH detectors at Belle II, 2017.

[57] T Kuhr, C Pulvermacher, M Ritter, T Hauth, and N Braun. The belle II core software. *Computing and Software for Big Science*, 3(1):1, 2019.

[58] A Koga, T. Selce and S. Stenge. Optimization of π^0 reconstruction selection and first systematic uncertainty of the efficiencies. URL: https://docs.belle2.org/record/1823/files/BELLE2-NOTE-PH-2020-003.pdf.

[59] Giovanni Punzi. Sensitivity of searches for new signals and its optimization. *arXiv preprint physics/0308063*, 2003.

[60] Catherine Bernaciak, Malte Sean Andreas Buschmann, Anja Butter, and Tilman Plehn. Fox-wolfram moments in higgs physics. *Physical Review D*, 87(7), Apr 2013.

[61] H Guler, H Aihara, K Arinstein, V Aulchenko, T Aushev, AM Bakich, V Balagura, E Barberio, K Belous, V Bhardwaj, et al. Study of the $K^+\pi+\pi^-$ final state in $B^+ \to J/\psi K^+\pi^+\pi^-$ and $B^+ \to \psi' K^+\pi^+\pi^-$. *Physical Review D*, 83(3):032005, 2011.

[62] Louis Lyons. Discovering the significance of 5 sigma, 2013.